View metadata, citation and similar papers at core.ac.uk
brought to you by CORE
provided by ScholarBank@NUS

Optical Characterizations of Nano-scaled Silicon

Zeng Yuping

(B. Eng, Jilin University, M. Sc, Jilin University)

A THESIS SUBMITTED

FOR THE DEGREE OF MASTER OF SCIENCE

DEPARTMENT OF PHYSIS

NATIONAL UNIVERSITY OF SINGAPORE

2004

Acknowledgement

I would like to express my sincere gratitude to my supervisors, Associate Professor Shen Zexiang and Associate Professor Lu Yongfeng, for their constant encouragement, invaluable guidance and gracious advice in the course of this research.

I would also like to express my greatest appreciation to other members of staff in the Physics Department and Department of Electrical and Computer Engineering. Special thanks go to Dr. Sun Wanxin and Dr. Yu Ting for their valuable discussion, suggestions and help in Raman and Photoluminescence Spectra and analysis. Thanks are also due to all the colleagues in Laser Spectroscopy Group and Laser Micro-processing Group as well as other postgraduates in Physics Department of National University of Singapore.

I sincerely acknowledge the research scholarship from National University of Singapore, which enables me to complete the research project and thesis.

Last but not least, I would like to thank my family for their love, encourage and support.

Optical Characterizations of Nano-scaled Silicon

Abstract

By Zeng Yuping
Supervisors: A/P Shen Zexiang, Department of Physics
A/P Lu Yongfeng: Department of Electrical and Computer Engineering

There are many techniques to investigate optical properties of semiconductor materials, such as Raman spectroscopy and photoluminescence spectroscopy, which are both non-destructive methods. In my project, Raman spectroscopy was used as a powerful tool to determine the recrystallization and thickness of amorphous silicon as well. The intensity of Raman spectra increases as the energy of the annealing laser incident on the amorphous layer is larger than 0.4 J/cm^2. A new method using the substrate Raman peak intensity to determine the thickness of the amorphous Si layer was investigated. In addition, photoluminescence spectroscopy was adopted to determine the strong light emission from nano-scale silicon prepared by excimer laser. Scanning Electron Microscopy was also used to map the nano-scale silicon. It was found that silicon oxide plays a key role in the luminescence and pulsed laser ablation could be one way to obtain silicon structures with strong light emission.

Summary

In this thesis, two main techniques, Raman and photoluminescence spectroscopy, were utilized to characterize the optical properties of amorphous Si and nano-structured Si materials.

In chapter one, we introduced the principles and mechanisms of Raman and PL spectroscopy, as well as their respective applications.

In chapter two, Raman spectroscopy was employed to characterize the re-crystallization of amorphous silicon after excimer laser annealing. It was found that laser fluence at 0.4 J/cm^2 is needed to re-crystallize the amorphous silicon layer. The Raman intensity of the c-Si peak decreases due to attenuation by the amorphous silicon layer. Besides the sharp Raman peak at 520 cm^{-1} due to the c-Si substrate, the samples also show a broad peak of the amorphous phase in the range of 480-520 cm^{-1}. The intensity of the c-Si Raman peak at 520 cm^{-1} varies with the angle between laser polarization and silicon crystal orientation. Based on this phenomenon, a method to calculate the thickness of amorphous silicon was developed with three different excitation light sources. It has been found that the thickness of our a-Si is about 18 nm, which was confirmed by SRIM (Stopping Range of Ions in Matter) result. Hence, it is demonstrated that Raman spectroscopy can be used to measure the thickness of the a-Si layer on c-Si substrate.

In chapters three and four, PL spectroscopy was used to characterize the light emission from silicon nano-structures. Excimer laser annealing ablation on silicon substrate

obtained different structures that give rise to strong light emission. The ambient under which the laser treatment was carried out showed much effect on the formation of the nano-structures. Previous literature showed that photoluminescence of more intensity and higher emission energy could be observed due to the oxidation of silicon nano-crystals. This contradicted our results which did not show any increase in PL. The mechanism behind it needs further investigation.

Contents

Summary 1

Chapter 1 Introduction to optical techniques and their applications 3

1.1 Introduction to Raman spectroscopy 3
1.1.1 Mechanism of Raman Spectroscopy 3
1.1.2 Comparison with IR spectroscopy 5

1.2 Introduction to Photoluminescence spectroscopy 7
1.2.1 PL mechanism 7
1.2.2 Intensity and full width at half maximum (FWHM) of PL spectrum 9
1.2.3 Wide-bandgap material effects on PL 10
1.2.4 Other factors that affect PL spectra 10

1.3 Applications of Raman spectroscopy 12

1.4 Applications of Photoluminescence spectroscopy 13
1.4.1 Bandgap determination 13
1.4.2 Impurity levels and defect detection 13
1.4.3 Recombination mechanisms 14
1.4.4 Material quality 14

Chapter 2 Excimer laser induced re-crystallization and thickness determination of amorphous silicon layer using Raman spectroscopy 16

2.1 Introduction to excimer laser 16

2.2 Introduction to Raman investigation on excimer laser annealing 17

2.3 Laser annealing literature review 18
2.3.1 Advantages of Laser annealing (LA) compared with RTA (Rapid thermal annealing) 18
2.3.2 Investigation on re-crystallization of amorphous silicon with laser annealing 20
2.3.3 Reversible transition from crystalline to amorphous state 21
2.3.4 Raman scattering from undersurface layers of ion implanted silicon crystals 22
2.3.5 Raman spectra of polycrystalline silicon by KrF excimer laser annealing 24

2.4 Ellipsometry principle 25

2.5 Experimental details 26

2.6 Results and discussions 28
2.6.1 Raman spectra 28
2.6.2 Calculation of a-Si layer thickness 28
2.6.3 Thickness determination-rotation experiment 35
2.6.4 Re-crystallization 41
2.6.5 Speculation on Raman intensity 42

2.7 Conclusions 43

Chapter 3 Theoretical estimations on nano-crystal 46

3.1 Theory of photoluminescence from nano-scale silicon 46
3.1.1 Effective Mass Model 46
3.1.2 Theoretical difficulties in modeling Si nano-crystals 47

3.2 Theoretical calculations 51

Chapter 4 Investigation on light emission from nano-scale Si 57

4.1 Motivation for achieving silicon nano-crystals 57
4.1.1 Opto-electronics 57
4.1.2 Single electron transistor (SET) 59

4.2 Mechanisms of photoluminescence from silicon nano-structures 61

4.3 Nano-scale silicon fabrications and typical results in literature 63
4.3.1 Porous silicon by electrochemical etching 63
4.3.2 Silicon pillars and cones by ion etching 64
4.3.3 Silicon nano-crystal prepared by silicon ion implantation into SiO_2 films 66
4.3.4 Silicon nano-clusters with reduced size dispersion produced by laser ablation 67
4.3.5 Photoluminescence from silicon single quantum wells 68
4.3.6 Silicon nanocrystals with sizes below 1.5 nm in Si/SiO_2 multilayers by LPCVD 71
4.3.7 Silicon nano-particles synthesized by laser-induced decomposition of silane 71
4.3.8 Silicon nano-colloids 72

4.4 Challenges 72

4.5 Experimental details 73

4.6 Experimental results and discussions 74

4.7 Conclusion 87

4.8 Future work 88

Chapter 1 Introduction to optical techniques and their applications

Raman spectroscopy and photoluminescence (PL) spectroscopy are powerful optical techniques for the characterization of materials. In this chapter, the Raman and PL spectroscopies and their applications are introduced.

1.1 Introduction to Raman spectroscopy

1.1.1 Mechanism of Raman spectroscopy

Laser Raman spectroscopy [1] deals with the measurement of vibrational states from a solid, liquid, or gaseous sample. Although any light source can be used, the intrinsically low intensity of Raman scattered radiation generally requires the use of laser radiation as the excitation source and, in fact the use of Raman spectroscopy has increased significantly since the development of high powered, continuous wave gas ion lasers in the late 1960's. Raman data are usually given as wavenumber (cm^{-1}) shifts from the incident radiation. The Raman shifts in wavenumbers are absolute energy differences between vibrational eigenstates of the molecule, and are not a function of the wavelength of the incident radiation.

Raman spectroscopy [2] is based on the detection of light that has been in-elastically scattered by a sample: the 'Raman effect'. In general, when light interacts with a substance it can do so in three main ways: the light may be absorbed, it may be transmitted through the sample unchanged or it may be scattered. Figure 1.1 illustrates the general principle of Raman scattering. The photons that are scattered elastically (i.e

without any change in their wavelength) comprise the Rayleigh scattering, which is intense but carries no vibrational information and so is filtered out of the signal. In addition to the Rayleigh scattering, Raman scattering, in which the frequency of the incident photons changes due to interaction with the sample, can also be detected. Unfortunately, the Raman comprise a very small fraction of the incident photons, typically 0.0001%, hence the need for an intense source and sensitive detector. Not all Raman-scattered photons have the same change in energy. First of all, some of photons lose part of their energy to give the Stokes scattering while others gain energy and generate the anti-Stokes signal. To generate an anti-Stokes signal the photons must encounter a vibrationally excited molecule in the sample, Stokes scattering has no such requirement so the Stokes signals tend to be stronger than the anti-Stokes and spectra are normally recorded only on the Stokes (energy loss) side of the spectrum. The Stokes photons energy loss reflects the vibrational levels within the sample. In practice, plotting the intensity of the Raman scattered photons against frequency difference between incident and scattered radiation maps the vibrational spectrum of the sample.

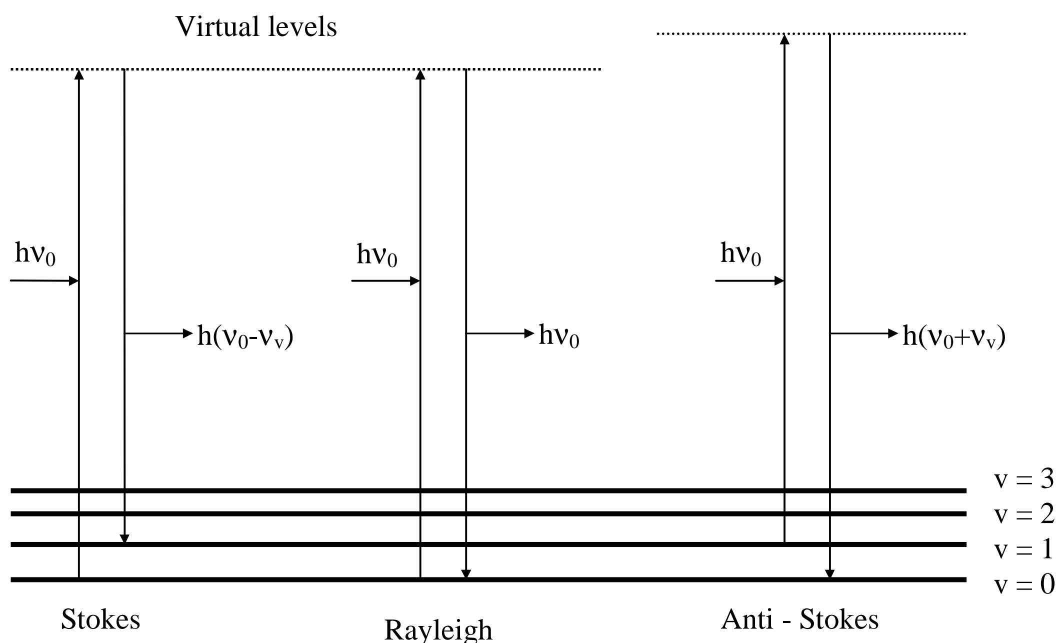

Fig. 1.1 Principle of Raman scattering

1.1.2 Comparison with IR spectroscopy

For quantitative analysis, Raman scattering intensity is linearly proportional to analyte concentration. Potentially, this feature may convey two significant advantages in analysis, particularly with respect to IR absorption techniques: (a) increased linear dynamic range, and (b) additivity of signals from multiple analytes. Traditionally, Raman analysis has been viewed as a relatively insensitive technique. Indeed, the probability of a molecule producing Raman scattering is much less than the probability of absorption in the IR region.

Direct correspondence can be made between the wavenumber shifts in vibrational Raman spectroscopy and those observed in infrared absorption spectroscopy. Thus, Raman scattering can also be used for qualitative identification of organic compounds using group frequencies and scatter intensities. However, the selection rules and relative intensities of infrared and Raman peaks are dissimilar, so that Raman and IR spectroscopies are often viewed as complementary. Furthermore, polarization measurements of Raman scatter can be used to gain information regarding the symmetry of vibrational modes using Raman, providing an additional dimension to the technique as compared with IR absorption methods.

Overall, the Raman and infrared (IR) signals measure the same vibrational levels (with subtly different selection rules). The major difference is that the presence of a vibrational band is detected in IR measurements directly by the absorption of an infrared photon, while in Raman experiments the same vibration causes the scattering of a photon which retains most of its energy but shows a small loss corresponding to the same energy

absorption by the sample as occurs in IR spectroscopy. Every compound has its own unique Raman spectrum, which can be used for both sample identification and quantification. Raman and IR spectroscopy can be used as complimentary techniques, because, due to differences in the spectroscopic selection rules, each is sensitive to different components of a given sample. As an example, IR spectroscopy is generally more sensitive to polar bonds, for example O-H stretches, whereas Raman is much more sensitive to vibrations of carbon backbone structures and symmetrical bonds, such as those in C=C groups. Using both techniques to characterize a particular substance can provide twice as much information on its chemical composition as would be obtained from using either of the techniques on their own.

However, advances in instrumentation have narrowed the gap considerably, to the point where, in some optimal cases, the sensitivity of normal Raman scatter compares favorably with IR absorption [3]. In addition, the Raman scattering efficiency can be greatly increased by use of the surface enhanced and resonance Raman effects. Raman spectroscopy is now a powerful analytical technique for a wide variety of applications, ranging from environmental analysis through industrial process control to biomedical diagnostics. Although Raman spectroscopy is increasingly being used for quantitative analysis, there are a number of obstacles to overcome before Raman techniques can routinely match the accuracy, precision, and ease of use of more mature analytical methods. Two important components of any reliable analytical method are reproducibility and sensitivity. In order to achieve high performance in these areas, a thorough understanding of the Raman scattering process, and of light scattering in general, is necessary.

1.2 Introduction to photoluminescence spectroscopy

1.2.1 PL mechanism

Photoluminescence [4] is a general term used to describe the effect observed following excitation with light photons. The time interval between excitation and emission, in turn, determines whether the process is fluorescence (almost instantaneous) or phosphorescence (delayed after glow). In fact, the emission characteristic of a particular body often contains a wide range of radiative lifetimes. The threshold energy required for photo-excitation, corresponds to the energy needed to transfer an electron from a bonding (valence) state to a non-bonding (conduction) state, and is thus equivalent to the energy

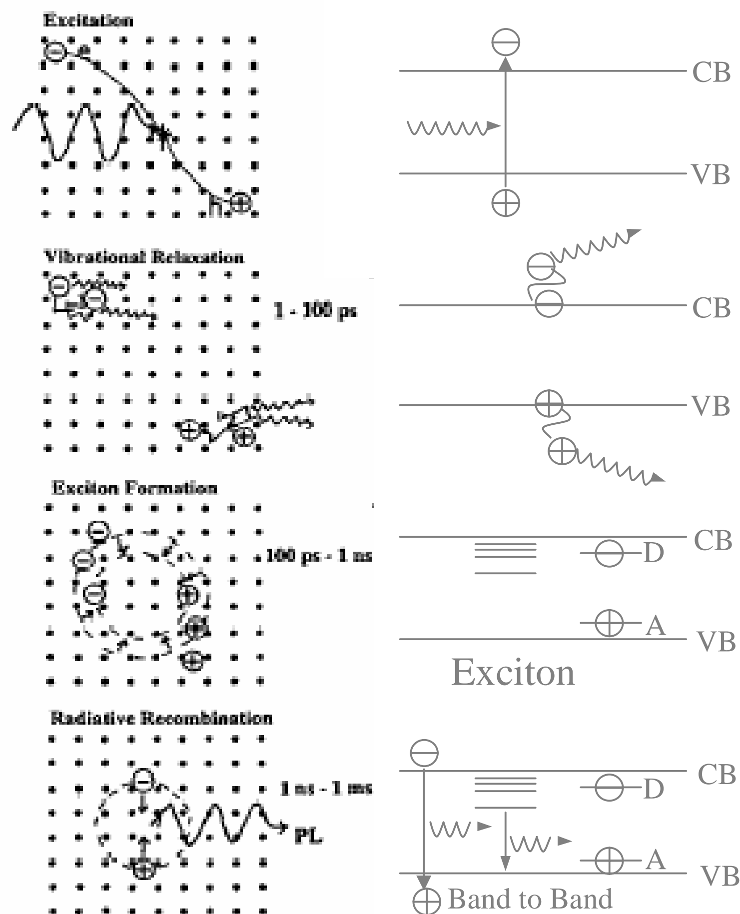

Fig. 1.2 Photo-excitation process

required to break a bond [5,6]. Figure 1.2 depicts the photo-excitation process in terms of both real space and energy levels. The transfer of an electron out of the valence band leaves behind an unoccupied level, or hole, which is positively charged. The PL process is then completed by the radiative recombination, and thus annihilation, of an electron-hole pair.

There are a number of separate recombination processes that can occur. These correspond to transitions involving free carriers, free carriers to donor or acceptor states, and those involving both free and bound excitons. Since donor-acceptor recombination involves carriers with localized wavefunctions, it can only take place directly by radiative tunneling between the two energy levels. As such, the PL energy will contain a Coulomb term, which reflects the physical separation, *r*, of the two trap sites in real space:

$$\hbar\omega = E_g - (E_A + E_D) - e^2 / 4\pi\varepsilon r$$

Where $\hbar\omega$ is the energy of the emitted photon, E_g the bandgap of the semiconductor, E_A and E_D the binding energies of acceptors and donors, respectively, and ε is the dielectric function of the material. In most cases, the wide distribution of donor-acceptor separations merely results in a broadening to the width of the PL band. However, in a few cases [7-8], the presence of well-defined donor and acceptor sites results in a PL spectrum containing a great deal of fine structure, and a wealth of information which can be deduced by fitting an appropriate donor-acceptor distribution function to the PL data. An exciton is formed when a photo-excited electron-hole pair is brought together by means of their mutual coulumb interaction. Since an exciton is electrically neutral, it can often diffuse over much greater distances than isolated charge carriers, without being either scattered or undergoing recombination. Moreover, the correlation of an electron with a specific hole means that an exciton can be described analogously to a hydrogen

atom, in terms of an electron and hole orbiting about a reduced center of mass. As such, there exists a certain binding energy which needs to be supplied in order to ionize the exciton, together with a characteristic physical extent to the exciton, defined in terms of an effective Bohr radius (typically 4-40nm). The excitonic radius does not play much of a role in bulk materials; however, it does enable PL measurements to become extremely sensitive probes of semiconductor interfaces, when the dimensions of the layer become comparable with that of the exciton. This is why PL was used in the characterization of our sample.

1.2.2 Intensity and full width at half maximum (FWHM) of PL spectrum

In addition to the peak energy of a particular PL transition, the intensity and full width half maximum (FWHM) values of the line-shape are of interest. Both parameters are affected by the quality of the crystal, in that a greater number of impurities, or defects, tend to both decrease the intensity, and increase the FWHM of the PL peak. The FWHM, in particular, reflects the lifetime of the carrier involved in the recombination process. It is inversely proportional to an effective lifetime, τ_{eff} , which is given by:

$$\frac{1}{\tau_{eff}} = \frac{1}{\tau_r} + \frac{1}{\tau_{nr}} + \frac{1}{\tau_s}$$

where τ_r is the radiative lifetime, τ_{nr} is the non-radiative lifetime arising from the bulk, and τ_s the non-radiative lifetime arising from the surface or interface. Hence, by appropriate selection of the sample structure, it is possible to focus on either bulk, or surface/interface recombination, independently of each other. For example, in the case of low to moderately-doped thick epitaxial layers, the electrical mobility will be inversely proportional to the FWHM of the PL signal.

1.2.3 Wide-bandgap material effects on PL

Interfacial recombination at a particular hetero-junction can be explored in detail if the sample is terminated with a wider bandgap material, which then acts as a mirror to prevent both free electrons and holes from reaching the surface. If the region of interest is now sandwiched between layers of wider bandgap material, it will form a potential well for either, or both, electrons and holes. As the width of the well region is reduced, a point is reached at which the motion of carriers becomes restricted to the plane of the well. In this manner, the degeneracy of the states has been partially lifted, and the population of the well can be described in terms of electron and hole gases with defined states of energy quantization. In the simplest case of a well with infinite potential walls, the allowed energy levels are given by:

$$E_n = \pi^2 \hbar^2 n^2 / 2m^* L^2$$

where m^* is the effective mass of the electron, L is the width of the quantum well(QW), and n is a quantum number describing the state of excitation. The refinement associated with the computing the energy levels within a well with finite barriers will not be dealt with here.

1.2.4 Other factors that affect PL spectra

Since the thickness at which a potential well begins to show quantum effects is similar to the size of the exciton radius, it follows that the shape of the exciton will become distorted or squeezed as the thickness of the QW is reduced. This physical extension of the exciton, in a direction parallel to the well interfaces, means that the excitonic luminescence will reflect the interfacial roughness. With the existence of large, monolayer-flat terraces at both interfaces, discrete components in the PL spectrum can be

related directly to monolayer fluctuations in thickness at the well interfaces. On the other hand, the absence of large terraces at either interface leads to a broadening of the PL line-shape. However, the presence of micro-roughness, at either or both interfaces, can also result in sharp luminescence features. In this case, the energy splitting between PL peaks does not relate directly to fluctuations in thickness, on a monolayer scale, and may vary between different positions on the sample. At this point, it is worth emphasizing the bearing that the choice of material system has on the interpretation of PL data from low-dimensional structures. The FWHM of the PL line-shape in bulk materials scales with the number of scattering centers presents. The addition of one or more interfaces requires that the interfacial roughness also be included in any calculation of the line broadening [9, 10]. Hence, as the thickness of a QW is reduced, one would expect intuitively the FWHM of the PL spectrum to increase as a result of the increased surface to volume ratio.

A final point relates to the sensitivity of PL measurements as a probe of interfaces in low dimensional structures. The luminescence corresponds to the recombination of all carriers photo-excited within a diffusion length of the well region and subsequently trapped in the well. This means that the signal is much stronger than that expected for recombination of carriers excited within the well region alone by direct absorption. Hence, at low temperatures, where thermal excitation of the carriers out of the well region becomes negligible, resolvable PL emission can still be observed even for ultra-thin (1-2 ML thick) QWs.

1.3 Applications of Raman spectroscopy

Raman spectroscopy was first employed for the analysis of biological samples as far back as the 1930's. However, due to the difficulties in obtaining high quality data its application in this area remained largely under-utilized. Generally, the study of intact biological samples using Raman spectroscopy only became widespread with the introduction of NIR FT-Raman instruments in the late 1980's, when there was a dramatic upsurge of activity in this field. The introduction of near-red diode laser-based dispersive instruments in the past few years has fuelled the growth in application of Raman methods most notably in the pharmaceutical and semiconductor industries.

Examples of cases where Raman spectroscopy has been applied in the investigation of biological samples include [2]:

- Quantitative histochemical analysis of human arteries;
- Cancer diagnosis;
- Characterization of gallstones and kidney stones;
- Diagnosis of metabolic disorders by taking Raman spectra of hair and nails;
- Hard tissue implant biocompatibility and in vivo recovery characteristics;
- Corneal dehydration in relation to impaired visual acuity;
- Imaging of cells, e.g. carotenoids in lymphocytes;
- Diagnosis of Alzheimers disease;
- Analysis of the stratum corneum in human skin in relation to the administration of therapeutic agents.

As we move into the 21st century, advanced nano-technology and biotechnology applications will become increasingly common. This emerging field of nano-

biotechnology has the potential to significantly enhance healthcare in the future. It also represents a new challenge for methods such as Raman spectroscopy, especially in relation to the sensitivity of the instruments, as we move from the micro to the nano-level. Raman spectroscopy has now become a very important and powerful analytical tool in many different areas of industry and academia. Its utility within the health and life science sector is now of particular significance, because it can provide selective, rapid and highly sensitive methods of analysis.

1.4 Applications of photoluminescence spectroscopy

Photoluminescence spectroscopy could be practically used in qualitative investigations for semiconductors and fast determination of alloy composition in ternary compounds (GaAlAs, GaInAs, AlInAs...), etc. Details are given as following[11]:

1.4.1 Bandgap determination

The most common radiative transition in semiconductors is between states in the conduction and valence bands, with the energy difference being known as the bandgap. Bandgap determination is particularly useful when working with new compound semiconductors.

1.4.2 Impurity levels and defect detection

Radiative transitions in semiconductors also involve localized defect levels. The photoluminescence energy associated with these levels can be used to identify specific defects, and the amount of photoluminescence can be used to determine their concentration.

1.4.3 Recombination mechanisms

The return to equilibrium, also known as “recombination” can involve both radiative and non-radiative processes. The amount of photoluminescence and its dependence on the level of photo-excitation and temperature are directly related to the dominant recombination process. Analysis of photoluminescence helps to understand the underlying physics of the recombination mechanism.

1.4.4 Material quality

In general, nonradiative processes are associated with localized defect levels, whose presence is detrimental to material quality and subsequent device performance. Thus, material quality can be measured by quantifying the amount of radiative recombination.

References

1. J.J. Laserna, *Modern Techniques in Raman Spectroscopy*, University of Malaga, Spain 1996

2. S.E.J. Bell and A.R. Boyd, *Raman Spectroscopy-An Overview of its Potential and Application*, Avalon Instruments Ltd

3. T.J. Vickers and C.K. Mann, *Analytical Raman Spectroscopy*, Grasselli and Bulkin (Eds.), Wiley-Interscience, New York 1991

4. J. F. McGilp D. Weaire C.H. Patterson (Eds.), *Linear and Nonlinear Optical Spectroscopy of Surfaces and Interfaces*, Springer-Verlag 1995

5. Curie, D.: *Luminescence in Crystals*, Methuen, New York, Wiley, London 1963

6. Klick, C. C., Schulman, H. In: Seitz, F., Turnbull, D., (eds.) *Solid State Physics,* vol. 5. p.100, Academic Press, New York 1957

7. Thomas, D. G., Gershenzon, M., Trumbore, F.A., *Physical Review* 133A (1964) 269

8. Reynolds, D.C., Litton, C.W., Park Y. S., Collins, T. C., *Journal of the Physical Society of Japan 21*, supp. (1966) 143

9. Singh J., Bajaj, K.K., *Journal of Applied Physics* 57 (1985) 5433

10. Lee S.M., Bajaj, K.K., *Applied Physics Letters* 60 (1992) 853

11. Http://inventors.about.com/library/inventors/blphotoluminescence.htm

Chapter 2 Excimer laser induced re-crystallization and thickness determination of amorphous silicon layer using Raman spectroscopy

2.1 Introduction to Excimer laser

Excimer Lasers are a family of high pressure, pulsed gas lasers which produce intense UV light with high efficiency and high peak power at several useful wavelengths. The source of the emission is a fast electrical discharge in a high pressure mixture of a rare gas (argon, krypton, zeon) and a halogen gas (fluorin or hydrogen chloride). The specific combination of the rare gas and the halogen determines the output wavelength of the laser. There are four common wavelengths: 193, 248, 308 and 351nm, as shown in Table 2-1. The excimer lasers are the best-known practical sources of intense deep-UV radiation. The short wavelength UV energy from excimer lasers causes high levels of electronic excitation in irradiated materials leading to bond breaking and photo-ablation. These and other unique properties of UV light have provided a very broad field of applications for excimer lasers.

Table 2-1 Excimer laser wavelength and corresponding energy

	λ (nm)	E (eV)
ArF	193	6.42
KrCl	222	5.50
KrF	248	5.00
XeCl	308	4.03
XeF	351	3.53

2.2 Introduction to Raman spectroscopy investigation on excimer laser annealing

With the reduction of circuit geometries in ultra-large scale integration (ULSI), ultra-shallow *pn* junction plays a key role on the performance of metal oxide semiconductor field effect transistor (MOSFET). Pre-amorphization implantation (PAI) was introduced as a means of minimizing or eliminating dopant channeling. Ion implantation as a space-conserving method of doping wafers was a useful tool to control the amounts of impurities. However, the high-energy ion beams cause damage to the crystalline surface which requires post-annealing [1]. Furnace annealing, rapid thermal annealing and laser annealing techniques have been studied for this purpose [2, 3]. Annealing using excimer lasers has been studied as a promising option [4-6] because excimer laser has larger beam size and higher beam energy density than other laser light sources. In addition, the crystallization of amorphous silicon can be carried out with low damage to the substrate, since the light absorption coefficient of amorphous silicon is high in the range of ultraviolet light emitted by the excimer laser and laser heating is limited to a thinner surface layer as a result. As the melting point of a-Si is lower than that of c-Si [7], pn junctions formed by laser annealing would be confined in the a-Si layer.

Raman spectroscopy is a powerful tool to investigate the optical properties of semiconductors [8]. Raman scattering can be widely used to examine damage that accompanies ion implantation, and can determine the effectiveness of annealing processes. As crystalline material becomes amorphous, its Raman scattering cross section changes, resulting in a change in the overall intensity of the corresponding Raman peaks. In addition, the sharp phonon modes characteristic

of crystalline material change to broad peaks if the material becomes amorphous. Hence Raman spectra can easily distinguish between the two states. In the case of silicon, the crystalline phase is characterized by a strong sharp Raman peak at 520 cm^{-1} while the corresponding peak is a broad Raman peak below 500 cm^{-1} for the amorphous phase. Raman phonon modes also carry highly detailed information about crystal orientation. Raman spectroscopy has also been used for thickness determination. P. Dhamelincourt et al [9] has shown that it was possible to measure samples thickness down to 10 nm with the use of signal from a good quality non-resonant Raman spectrum. Thickness determination, thin film uniformity and local film orientation have also been studied by micro-Raman spectroscopy [10, 11].

In this study, we used Raman spectroscopy to investigate the re-crystallization of amorphous silicon annealed by an excimer laser. As the amorphous silicon crystallizes, the c-Si Raman peak intensity increases. The Raman spectra of the c-Si samples with and without amorphous layer were measured using three different excitation light wavelengths and the thickness of the amorphous layer was determined.

Some typical literature was reviewed at the same time we did our experiments.

2.3 Laser annealing literature review

2.3.1 Advantages of Laser annealing (LA) compared with RTA (Rapid thermal annealing)

Current rapid thermal annealing (RTA) faces the problems of thermal diffusion and low dopant activation that are limited by thermal budget and solid solubility, respectively. Laser annealing process has been reported to be an alternative to RTA. Since a laser pulse melts the Si surface within a few nano seconds and the melt recrystallizes within 10 ns, and abrupt profile is formed with no dopant diffusion beyond the solid/liquid interface, and high dopant activation (even above solid solubility) is achieved. A pulsed 308 nm, XeCl excimer laser beam scans across the wafer chip by chip [12]. Figure 2.1 shows the sheet resistance of boron implanted wafer (B^+, 7KeV, 10^{16} cm^{-3}) followed by either LA(0.25~0.40J/cm^2) or RTA(1000˚C,10 S). Power of 0.3 J/cm^2 is enough to achieve a low sheet resistance.

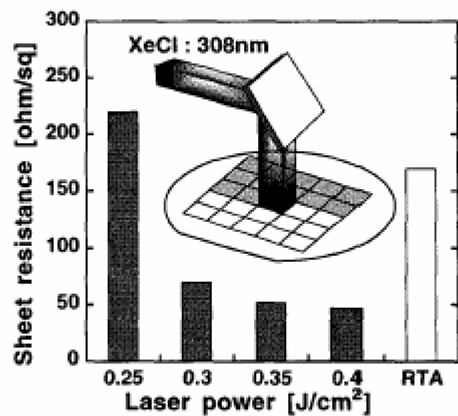

Fig.2.1 Sheet resistance with various LA power comparing with RTA (1000˚C, 10 Sec) [12]

2.3.2 Investigation on re-crystallization of amorphous silicon with laser annealing

Laser re-crystallization of amorphous silicon (a-Si) film is successfully used for producing crystalline films on insulating substrates for devices such as flat panel displays. One series of a-Si films, 10 nm to 386 nm thick, was irradiated homogeneously with different laser intensities and analyzed by Raman scattering [13]. Figure 2.2 shows three threshold intensities: The smallest belonging to re-crystallization of the a-Si film, and intermediate intensity yielding amorphous solidification of the molten film (initially amorphous or re-crystallized) and the largest causing fragmentation with microcrystalline solidification. Re-crystallization occurs above a threshold surface temperature. Therefore the re-crystallization intensity is nearly independent of film thickness when the film is thicker than 10 nm. For amorphization or film fragmentation, the entire film has to melt and the required intensities increases with film thickness.

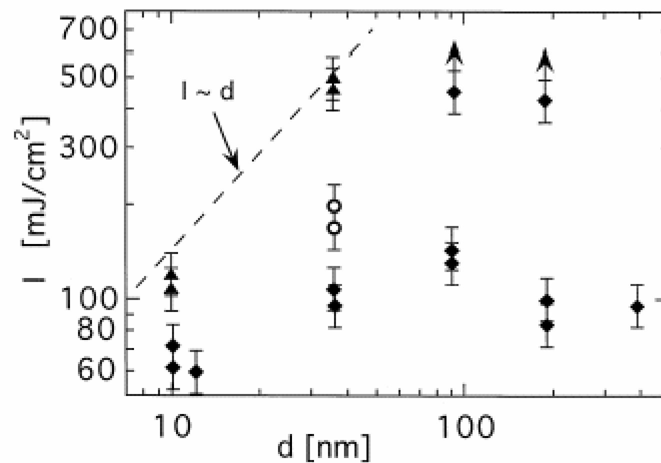

Fig. 2.2 Intensity I necessary for recrystallization(diamonds), amorphization (circles), and fragmentation (triangles) at varying film thickness d. The light penetration depth is 10 nm in both a-Si and μc-Si [13].

2.3.3 Reversible transition from crystalline to amorphous state

The reversible transition from crystalline to the amorphous state was observed by Raman scattering measurements [14]. Figure 2.3 shows TO phonon Stokes spectra for the 20-nm-thick un-doped silicon film. The as-deposited a-Si:H film spectrum had a broad TO phonon peak around 500 cm^{-1} and a tail on the lower energy side, which were assigned to the amorphous mode by Iqbal and Veprek [15] as shown by curve A. After crystallization by the initial irradiation, the spectrum shows a sharp TO phonon peak around 513 cm^{-1}, as shown by curve B. The sample was then amorphized by irradiation with a pulse at an energy density of 260 mJ/cm^{-2}. The spectrum showed a broad peak (curve C) which is similar to that of the as-deposited a-Si:H film (curve A). The laser-induced amorphized film was re-crystallized by irradiation with a pulse with an energy density of 220 mJ/cm^2. The spectrum again showed a sharp TO phonon peak around 510 cm^{-1} (curve D).

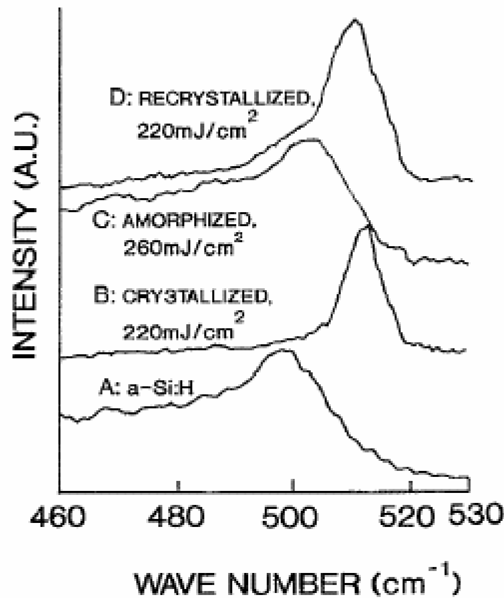

Fig.2.3 Raman scattering spectra for 20-nm-thick as-deposited a-Si:H film(A), crystallized by irradiation at 220mJ/cm^2 (B), amorphized by irradiation at 260 mJ/cm^2 (C), re-crystallized by irradiation at 220 mJ/cm^2 (D). Curves B, C, and D have zero offsets, respectively [14].

2.3.4 Raman scattering from undersurface layers of ion implanted silicon crystals

Raman scattering experiments of ion implanted and pulsed laser annealing (PLA) silicon were performed in the backscattering geometry at room temperature using various laser wavelengths [16]. Silicon <100> samples were ion implanted with 100 keV As^+, 50 keV B^+, and 50 keV P^+ to doses ranging from 10^{12} to 10^{15} ions/cm^2. Below the implant fluence of 3×10^{14} ions/cm^2, the Raman spectra of implanted silicon with diminished oscillator strength of two phonon modes are quite similar to the reference spectrum of un-implanted silicon as depicted in Figs. 2.4 (a), (b) and (c). An abrupt transition from crystalline state to amorphous state is observed in Figs 2.4 (d), (e) and (f) as the fluence is increased beyond 3×10^{14} ions/cm^2. Raman spectra of Figs 2.4 (e) and (f) show the formation of amorphous silicon. In addition to the usual broad peak (~470 cm^{-1}) of amorphous silicon, there is a crystalline peak at 518 and its overtone below 1000 cm^{-1} as shown in Fig. 2.4 (d). One can note in Fig. 2.4 (d)~(f) that there is a relatively quick disappearance of the overtone peak for a small increase of fluence above 3×10^{14} ions/cm^2.

It was observed that at small implantation doses only the decrease of the Raman intensity had taken place. Such result was explained as due to point defect, emerging in crystals after the ion implantation processes. When the ion implantation dose increases the additional Raman satellites were observed. Such satellites were associated with the crystalline lattice disordering and correlated with the one-photon density of states pecularities. The dose value of the whole lattice disordering depended from the mass and kind of ions.

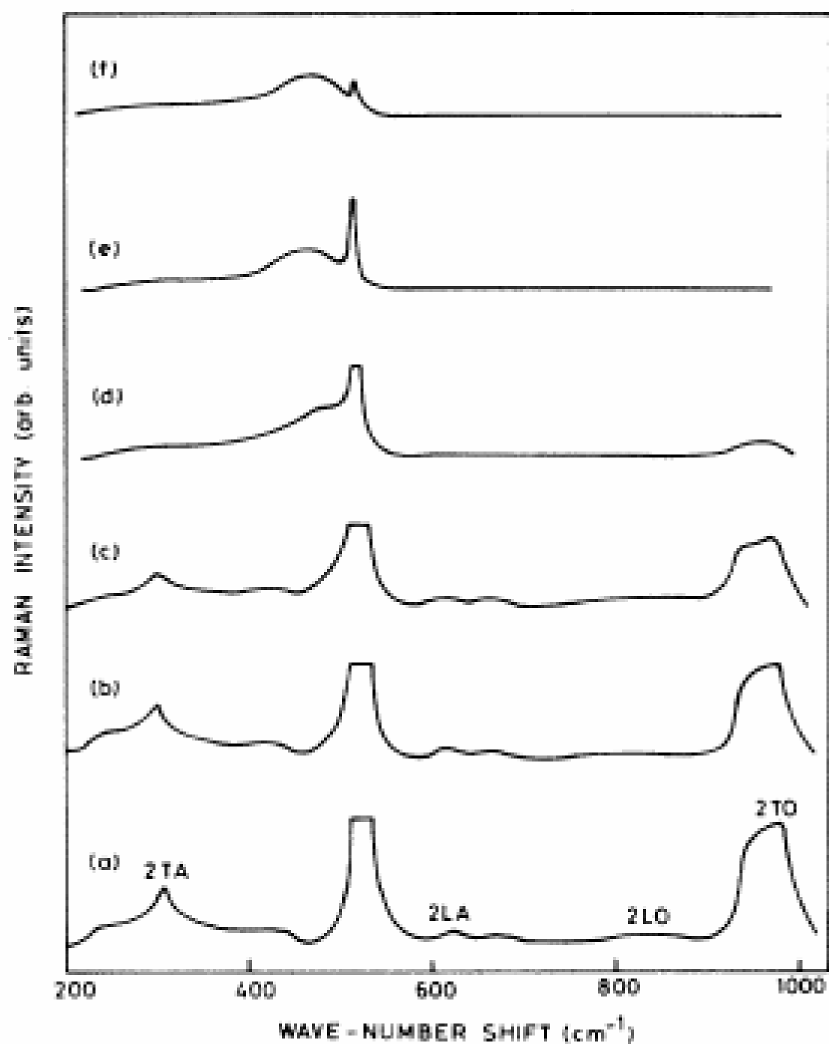

Fig. 2.4 Room-temperature backscattering Raman spectra with 514.5 nm laser line [16]. (a) Spectrum of pure silicon: (b), (c), (d), (e), and (f) spectra of silicon samples implanted with P^+ to the fluences of 1×10^{12}, 1×10^{14}, 3×10^{14}, 5×10^{14} and 1×10^{15} ions/cm^2, respectively. The spectra are arbitrarily cut off at the top of the one-phonon line to focus the attention on second-order spectra.

2.3.5 Raman spectra of polycrystalline silicon by KrF excimer laser annealing

The growth of a-Si films (100 nm thick) on the SiO_2 layer was carried out in an LPCVD reactor using a SiH_4 gas source at 420°C under the pressure of 30 Pa [17]. Figure 2.5 shows Raman spectra of a-Si and poly-Si crystallized at laser fluence of 0.2-0.8 J/cm^2. For comparison, the spectra from single-crystalline Si and furnace-annealed poly-Si are also included. The spectrum of as-deposited a-Si has a broad peak maximum near 480cm^{-1}.

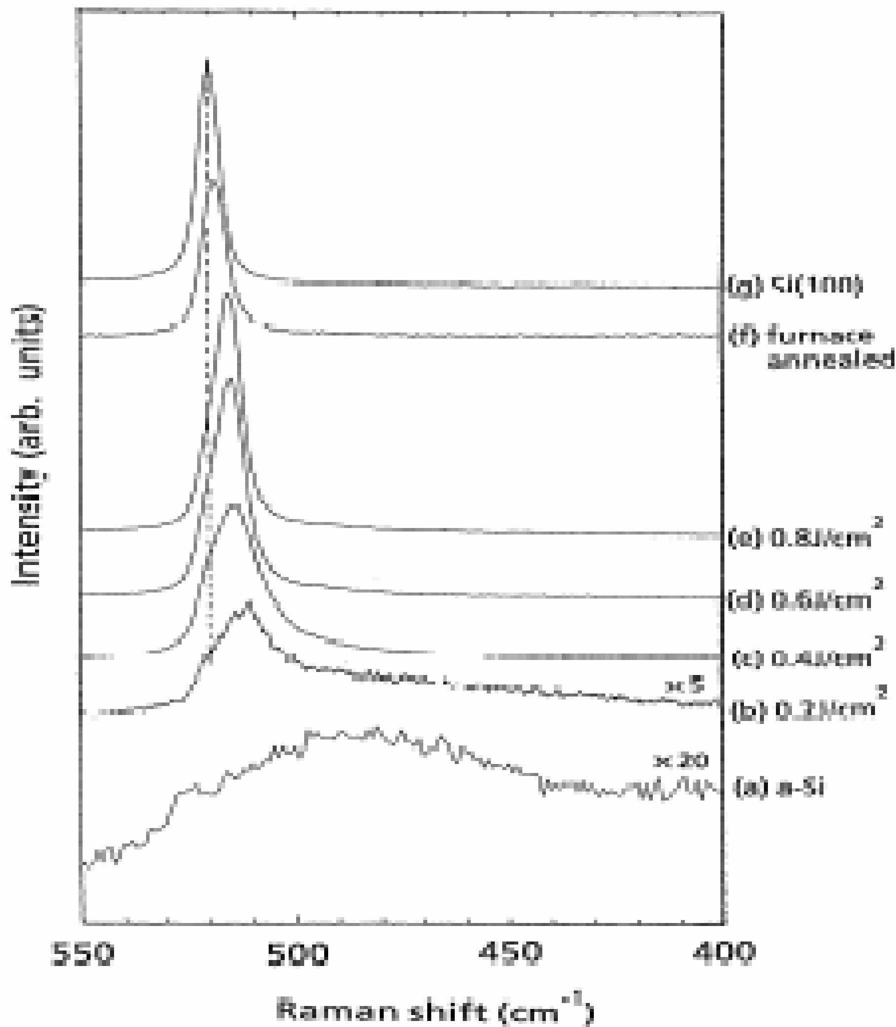

Fig. 2.5 Raman spectra for (a) a-Si and poly-Si crystallized at (b) 0.2 J/cm^2, (c) 0.4 J/cm^2, (d) 0.6 J/cm^2 and (e) 0.8 J/cm^2, and (f) furnace annealed poly-Si film (900°C, 24h) and (g) Si (100)[17].

The spectrum of poly-Si at 0.2 J/cm^2 shows essentially two components: a relatively sharp peak and a tail. The sharp component around 510-520 cm^{-1} can be assigned to the k=0, Γ_{25} optical phonon of crystalline Si. The tail corresponds to amorphous-like Si. The Raman shift of the Γ_{25} phonon line correlated with laser energy. Since Raman shift of crystalline Si decreased with an increase of compressive stress of films, the relationship between the stress of poly-Si and laser energy can be observed.

2.4 Ellipsometry principle

Ellipsometry is a method of using reflected light to determine properties of surfaces and materials. Polarized light is reflected at an oblique angle to a surface as shown in Figure 2.6. It usually consists of a monochromatic light source (eg. He-Ne laser), polarizer P, sample S, compensator C and second polarizer P' (C and P' often referred to as analyzer A), and detector D.

P ensures that equal amounts of s and p components of incident light reach S. On reflection, C and P' measure the phase difference and amplitude ratio of the s and p components, respectively. The change from a linearly polarized state to a generally elliptically one is measured. From these measurements, the thickness of the material or the complex index of refraction can be determined. The elliptical state is caused by the fact that the medium is not a perfect dielectric. It has a complex index of refraction and therefore absorption properties. The Maxwell boundary conditions are for a discrete boundary (perfect dielectric) between the air and the surface. Real dielectrics can be considered as a continuous boundary and new boundary conditions can be determined.

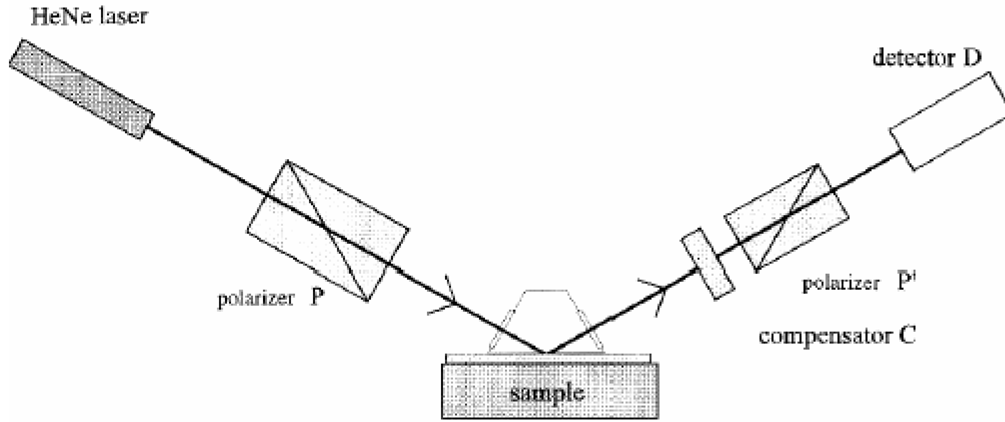

Fig. 2.6 Basic components of an ellipsometer[18]

From Fresnel equations governing the physical amplitudes and phases of the electric fields for reflected and refracted (transmitted) waves, we could obtain $\frac{n_1}{n_0} = \sin\varphi_0[1 + \frac{(1-\rho)^2}{(1+\rho)^2}\tan^2\varphi_0]^{1/2}$

where n_1, n_0 are the refractive index of the medium, φ_0 is the incident angle, ρ is the ratio of the complex Fresnel reflection coefficient. Knowing n_0 and measuring ρ and φ_0 , n_1 can be determined.

2.5 Experimental details

In our experiments, the samples were subjected to pre-amorphization implantation(PAI) of Si^+ ions at 10 keV with a dose of $1\times10^{15}/cm^2$. Subsequently, B^+ ion implantation was carried out at 0.6keV with a dose of $5\times10^{14}/cm^2$. The choice of B^+ ion implantation condition is typical of the P^+ source/drain extension junctions for the 100 nm technology node. C-Si wafers without implantation were used as reference samples. Crystallization of the amorphous layers was carried out using KrF excimer laser annealing at a wavelength of 248 nm and beam energy 0.2-0.5 J/cm^2.

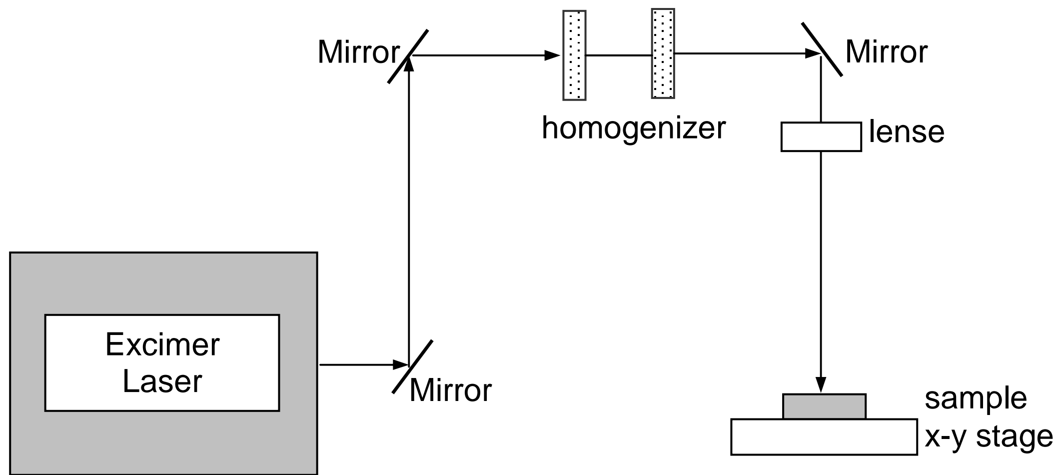

Fig. 2.7 The schematic representation of experimental KrF excimer laser annealing

The pulse width of the laser beam is 23 ns and the repetition frequency was 1 Hz. The experimental set up is schematically shown in Fig. 2.7. The laser annealing was performed at room temperature in air ambient. The samples were characterized by Raman spectroscopy at room temperature using three different laser excitation wavelengths, 488, 514.5 and 632.8 nm. In order to determine the thickness of the amorphous silicon, Raman spectra were recorded with the c-Si and a-Si/c-Si samples in two different methods: One method is to record the Raman spectra in a particular sample orientation relative to the laser polarization; The other is to change the angle between the orientation of the sample and the laser polarization using a rotation stage to obtain a relationship between the c-Si Raman intensity and the angle, which is then used to calculate the thickness of the amorphous layer. As the extinction co-efficient of a-Si is strongly dependent on the sample preparation method and parameters, different values of extinction coefficient were reported in the literature. In our study, ellipsometry was used to obtain the extinction co-efficient of our a-Si samples and thus the absorption coefficient was derived.

Computer simulation is used to estimate the projected range of the 10 keV Si^+ in c-Si. The results agree well with our thickness result derived from Raman spectra.

2.6 Results and discussions

2.6.1 Raman spectra

Figure 2.8(a) shows typical Raman spectra of a-Si/c-Si samples annealed under different laser fluence. The broad peak at ~480 cm^{-1} shown in figure 2.8(b) belongs to amorphous silicon [17, 19] and the strong and sharp peak at 520 cm^{-1} is due to crystalline c-Si. In the a-Si/c-Si samples, this peak arises due to the c-Si substrate and its intensity is attenuated by the a-Si layer which absorbs both the laser impinges on the substrate and the Raman signal from the substrate. This attenuation of the substrate Raman signal can be used to determine the a-Si layer thickness and the intensity increase of this peak in the laser-annealed samples gives a quantitative measure of the crystallization process.

2.6.2 Calculation of a-Si layer thickness

We used two methods to calculate the thickness of the a-Si layer. The first method uses directly the attenuation due to the a-Si layer for a particular c-Si orientation, by comparing the c-Si substrate Raman peak at 520 cm^{-1} with and without the a-Si layer. For the c-Si reference sample, let I_{R0} be the Raman scattering intensity detected by the spectrometer and I_0 the intensity of the

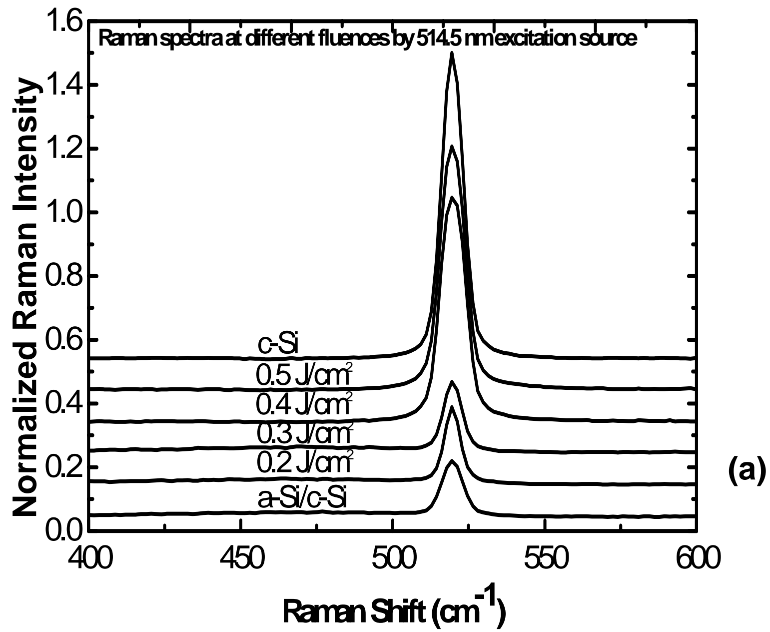

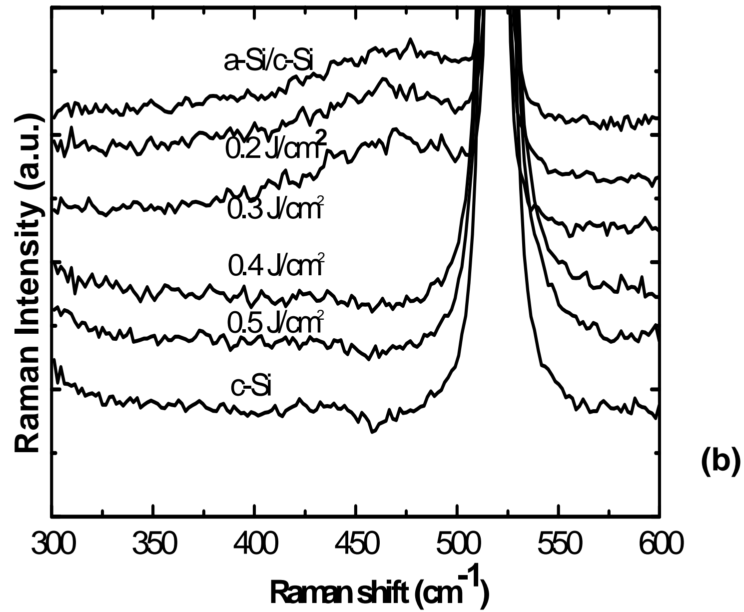

Fig. 2.8 The spectra of as-implanted sample and laser annealed samples in comparison with c-Si by 514.5 nm excitation light source. Amorphous silicon sample was prepared with Si^+ dose of 1×10^{15} at the implantation energy of 10KeV.

incident laser. Then the collected Raman signal I_{R0} is proportional to I_0. For a sample with an a-Si layer of absorption coefficient α_a and thickness t, Fig. 2.9 illustrates schematically the Raman scattering process for the c-Si substrate with a-Si on the top.

The laser has to pass through the a-Si layer to reach the Si substrate and the laser intensity I_t at the a-Si /c-Si interface is given by,

$$I_t = I_0 \exp(-\alpha_a t) \quad (1)$$

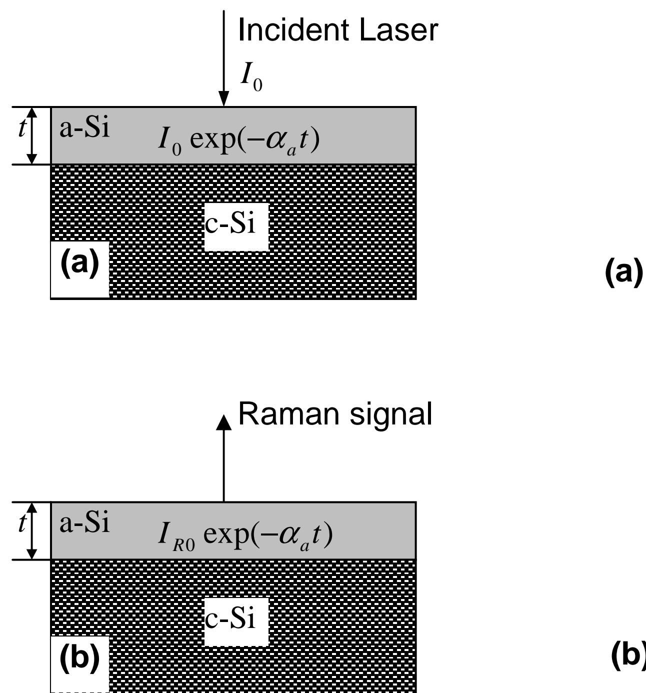

Fig. 2.9 (a) Incident laser (b) Scattered laser with c-Si substrate with a-Si layer. Amorphous silicon sample was prepared with Si^+ dose of 1×10^{15} cm^{-2} at the implantation energy of 10KeV.

Note that we assume $\alpha_a = \alpha_{Raman}$, where α_{Raman} denotes the absorption coefficient of the Raman signal by the amorphous silicon, because the wavelength difference between the laser and Raman signal is small.

Hence, the corresponding Raman signal is given by $I_{R0} \exp(-\alpha_a t)$. This Raman signal has to pass through the amorphous layer again before it can be detected by the spectrometer. Hence the Raman intensity entering the spectrometer is

$$I_{Ra} = I_{R0} \exp(-2\alpha_a t) \quad (2)$$

The absorption coefficient of a-Si can be quite different for samples prepared using different methods, as illustrated by refs. 20 and 21 (shown in Table 2-2). Table 2-2(a) shows higher absorption coefficient than (b). In this experiment it is determined from the extinction coefficient using ellipsometry, as shown in Fig. 2.10, and the absorption coefficients at different wavelengths are calculated according to $\alpha = \frac{4\pi k}{\lambda}$ using the extinction coefficients in Fig. 2.10. The calculated α_a value at 488, 514.5 and 632.8 nm is listed in Table 2-3. Therefore, the ratio of collected Raman signal intensity from the two samples with and without the a-Si layer is

$$\frac{I_{Ra}}{I_{R0}} = \exp(-2\alpha_a t) \quad (3)$$

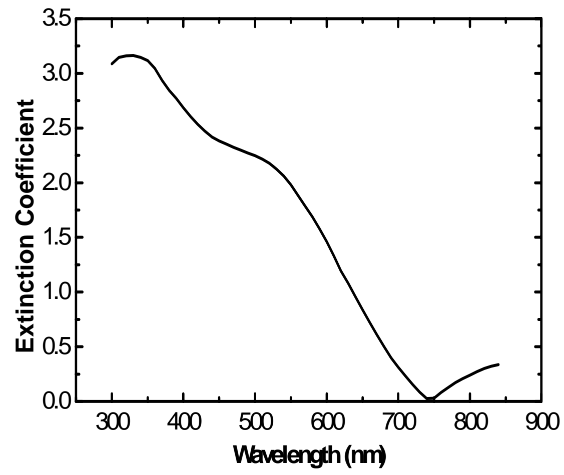

Fig. 2.10 Extinction coefficient as a function of wavelength of a-Si/c-Si measured by ellipsometry

Table 2-2 n and k of amorphous silicon from (a) ellipsometer model [20]and (b) handbook [21]

(a)

nm	n	k
300	3.6877	3.7673
320	4.1302	3.5205
340	4.6051	3.2539
360	4.7551	2.8008
380	4.9349	2.3579
400	5.0157	2.0009
420	5.0412	1.7019
440	5.0318	1.4494
460	5.0002	1.236
480	4.955	1.0556
500	4.9018	0.90321
520	4.8446	0.77438
540	4.786	0.66542
560	4.7279	0.57317
580	4.6715	0.49496
600	4.6173	0.42855
620	4.5658	0.37205
640	4.5174	0.3239
660	4.4719	0.28278
680	4.4294	0.24759
700	4.3898	0.21742

(b)

µm	n	k
0.1033	0.327	0.726
0.1078	0.363	0.847
0.1127	0.392	0.946
0.1181	0.423	1.04
0.124	0.459	1.14
0.1305	0.497	1.24
0.1378	0.543	1.35
0.1459	0.597	1.47
0.155	0.66	1.6
0.1653	0.735	1.74
0.1771	0.832	1.89
0.1907	0.951	2.07
0.2066	1.11	2.28
0.2254	1.35	2.51
0.248	1.69	2.76
0.2583	1.86	2.85
0.2695	2.07	2.93
0.2818	2.3	2.99
0.2952	2.56	3.04
0.31	2.87	3.06
0.3263	3.21	3
0.3444	3.55	2.88
0.3543	3.73	2.79
0.3647	3.9	2.66
0.3875	4.17	2.38
0.4133	4.38	2.02
0.4428	4.47	1.64
0.4769	4.49	1.28
0.496	4.47	1.12
0.5166	4.46	0.969
0.5636	4.36	0.69
0.6199	4.23	0.461
0.6526	4.17	0.363

Table 2-3 Thickness determination of amorphous silicon on silicon substrate

Parameters used to calculate a-Si thickness			
λ(nm)	488	514.5	632.8
k_a	2.28	2.19	1.077
α_a (nm^{-1})	0.0587	0.0534	0.0214
Calculation without rotation			
$\ln(I_c / I_a)$	2.173	1.876	0.7804
t(nm)	18.51	17.56	18.23
Calculation with rotation			
$\ln(\frac{I_{c\max} - I_{c\min}}{I_{aman} - I_{a\min}})$	2.023	1.730	0.778
t(nm)	17.23	16.20	18.18

2.6.3 Thickness determination-rotation experiment

We have also recorded Raman spectra as a function of the laser polarization. This experiment allows us to determine the thickness of the a-Si layer for the a-Si/c-Si samples and to derive information about the grain orientation of the re-crystallized samples. We first derive the angle dependence of the Raman peak below.

Assume the electrical field of the incident laser is along the *x*-axis in the laboratory coordinate system i.e. $\begin{pmatrix} E_0 & 0 & 0 \end{pmatrix}$ and the *b* axis of the Si crystal makes an angle θ with the laser polarization (i.e. the *x*-axis of the laboratory system). In the experiment, the angle θ is varied by rotating the crystal with respect to the *c* –axis which is also the *z*-axis of the laboratory system. With such experimental arrangement, only the *x* and *y* components of the Raman signal are detectable, which are given by,

$$\begin{pmatrix} \cos\theta & -\sin\theta \\ \sin\theta & \cos\theta \end{pmatrix} \begin{pmatrix} 0 & d \\ d & 0 \end{pmatrix} \begin{pmatrix} \cos\theta & \sin\theta \\ -\sin\theta & \cos\theta \end{pmatrix} \begin{pmatrix} E_0 \\ 0 \end{pmatrix} = \begin{pmatrix} dE_0 \sin 2\theta \\ dE_0 \cos 2\theta \end{pmatrix} . \tag{4}$$

(Matrix $\begin{pmatrix} \cos\theta & \sin\theta \\ -\sin\theta & \cos\theta \end{pmatrix}$ is multiplied for the in-comimg laser signal from its original co-ordinate to change into the crystal co-ordinate, then we multiply by $\begin{pmatrix} 0 & d \\ d & 0 \end{pmatrix}$ to let laser interact with crystal. After that, we multiply by matrix $\begin{pmatrix} \cos\theta & -\sin\theta \\ \sin\theta & \cos\theta \end{pmatrix}$ to let the coming out Raman signal from the crystal co-ordinate to change back into the original co-ordinate).

In a real experiment, the Raman spectrometer may have different responses in x and y polarizations, which are set as k and unity, respectively. Hence the observed Raman intensity I in the x and y polarization can be written as, respectively,

$$
\begin{aligned}
I_x &= kE_x^2 = kd^2 E_0^2 \sin^2 2\theta \\
I_y &= E_y^2 = dE_0^2 \cos^2 2\theta
\end{aligned}
\tag{5}
$$

If un-polarized Raman spectra are recorded, the overall intensity is then given by,

$$
\begin{aligned}
I &= I_x + I_y \\
&= kd^2 E_0^2 \sin^2 2\theta + d^2 E_0^2 \cos^2 2\theta \\
&= \frac{d^2 E_0^2}{2}(1-k)\cos 4\theta + \frac{d^2 E_0^2}{2}(1+k)
\end{aligned}
\tag{6}
$$

The Raman intensities show a sinusoidal dependence on θ with a period of 90°. Similarly, the intensity of the a-Si sample shows the same θ dependence, except an additional factor $e^{-2\alpha t}$ due to attenuation of both the laser and Raman signal by the amorphous layer as mentioned before.

Figure 2.11 shows the un-polarized Raman spectra as a function of angle θ, recorded with an Ar ion laser at different wavelengths. The Raman intensity for both the a-Si/c-Si and c-Si samples showed a period of 90° as expected. It is easy to show that the thickness t of the amorphous layer can be derived from the following expression,

$$
\frac{I_{a-\max} - I_{a-\min}}{I_{c-\max} - I_{c-\min}} = \exp(-2\alpha_a t) \tag{7}
$$

Where $I_{a-\max}, I_{a-\min}, I_{c-\max}, I_{c-\min}$ are the measured maximum and minimum Raman intensity of amorphous silicon and crystal silicon, respectively, which can be taken from Fig. 2.11. The calculated thickness t using eq. (3) is 18.10±0.36 nm and the result using eq. (7) is 17.20±0.67 nm. The schematic calculation is shown in Fig. 2.12. It is obvious that both results agree with

each other very well. It is also confirmed by the SRIM result shown in Figure 2.13. We used SRIM software to calculate the project range of Si^+ into silicon, and the result showed that the project range increases as the ion implantation energy increases. When ions impinge on a target, they lose kinetic energy due to collisions with the nuclei and electrons of the target material. The extent to which the ions can move strongly depend on their mass and energy they possess. The project range at 10 keV obtained from our SRIM result is 17.4 nm, which is consistent with the result obtained in [22]. This demonstrates that determination of a-Si layer thickness using Raman spectroscopy is practical.

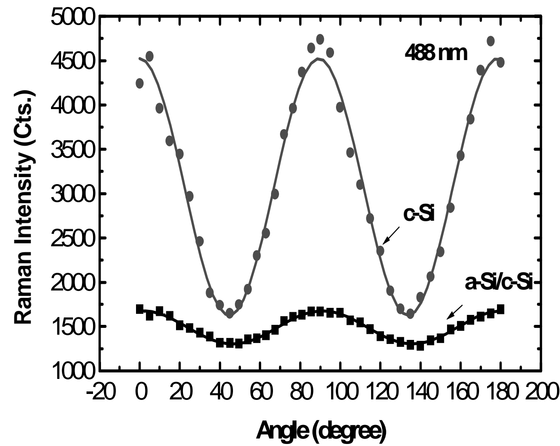

(a)

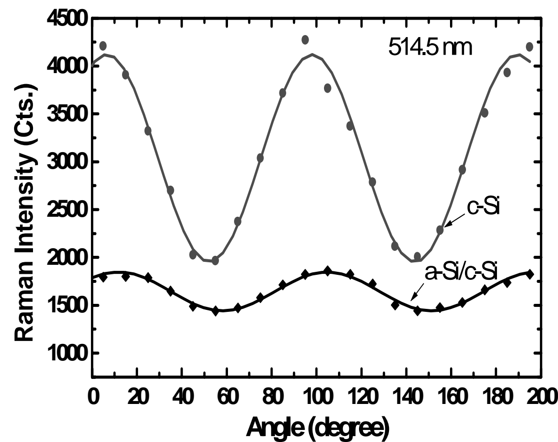

(b)

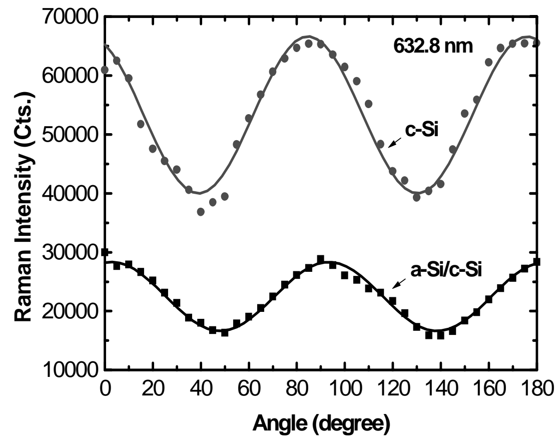

Fig. 2.11 Raman intensity of the c-Si substrate as a function of angle between laser polarization and crystal orientation for an a-Si/c-Si sample and c-Si reference sample at three different wavelengths (a)488 nm (b) 514.5 nm (c) 632.8 nm

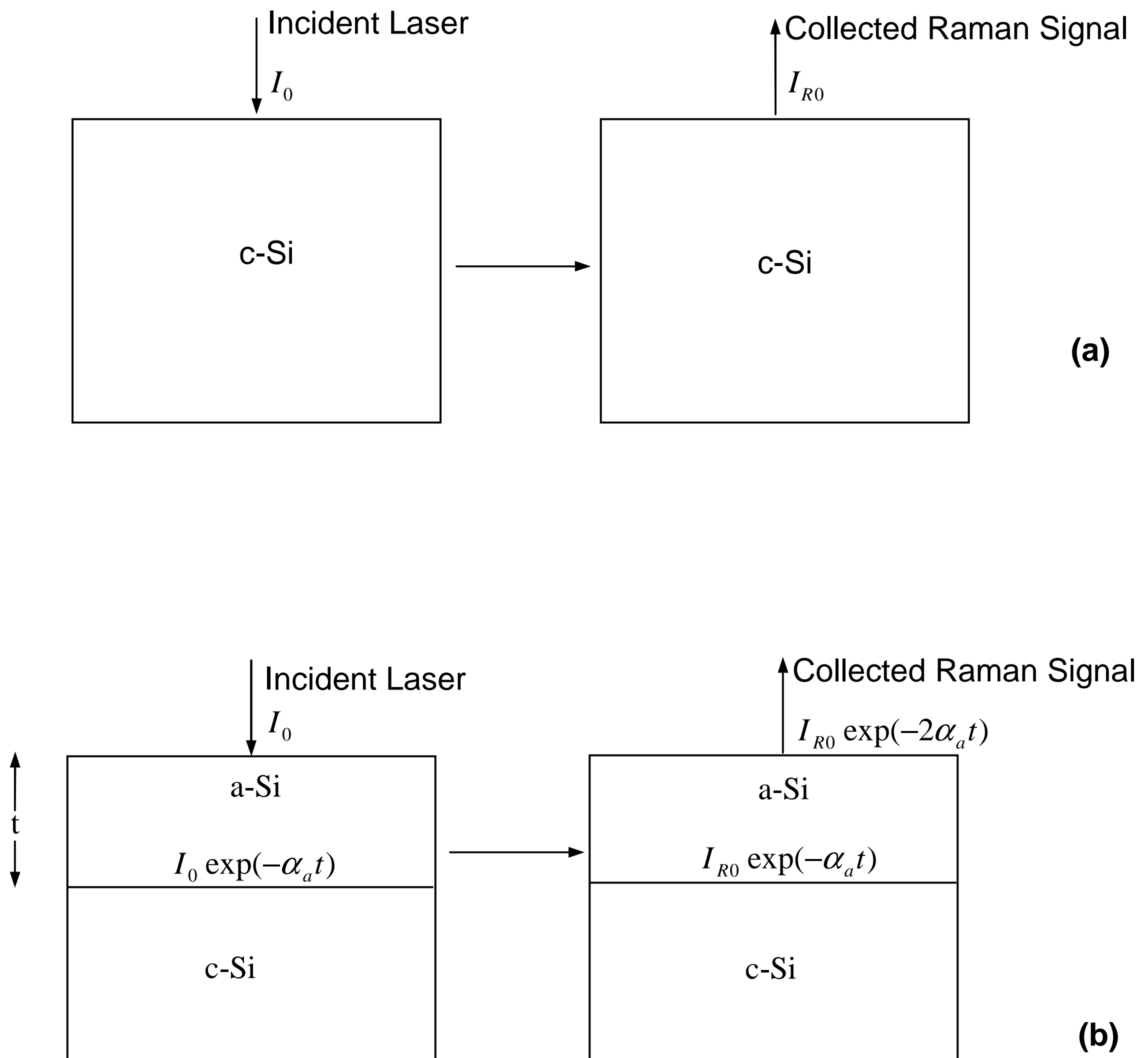

Fig. 2.12 Schematic representation of a-Si thickness calculation (a) c-Si (b) a-Si/c-Si

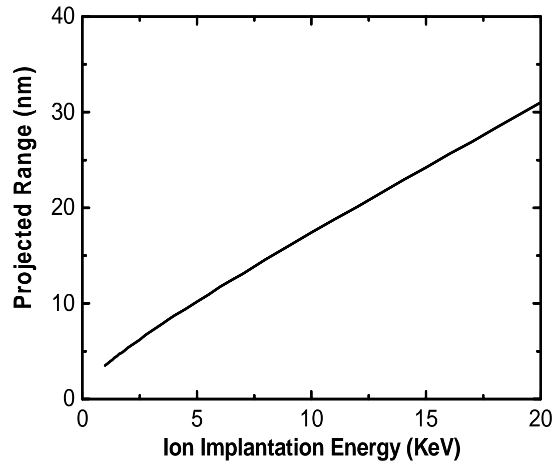

Fig. 2.13 SRIM simulation result of projected range as a function of ion implantation energy sample

2.6.4 Re-crystallization

As shown in Fig. 2.8, the characteristic a-Si peak at ~480 cm^{-1} is present for the pre-annealed sample and samples annealed at the fluence below 0.3 J/cm^2. This peak is absent for samples annealed with higher laser fluence, indicating the fluence of 0.4 J/cm^2 is enough to re-crystallize the a-Si samples. Similarly, the Raman signature of c-Si which consists of a strong narrow peak located at 520 cm^{-1} is stronger for the samples annealed at laser fluence of 0.4 J/cm^2 or higher. We have also attempted to use glancing angle x-ray diffraction to study the a-Si/c-Si samples. However we only succeeded in observing the XRD peaks of the c-Si substrate. The reason is that the a-Si layer is too thin in addition to the fact that XRD peaks of a-Si are weak and broad. It again shows the advantage of using Raman spectroscopy to distinguish crystalline state from amorphous state.

2.6.5 Speculation on Raman intensity

As shown in figure 2.8, samples annealed at 0.2 J/cm^2 and 0.3 J/cm^2 show much lower peaks at 520 cm^{-1} than samples annealed at 0.4 J/cm^2 and 0.5 J/cm^2 do. It is supposed that, in the high fluence region 0.4-0.5 J/cm^2, as shown in Fig. 2.14, because the melting point of a-Si was 200~300°C below the crystal melting temperature (1414°C) [23], the a-Si thin layer is entirely melted when it is irradiated by high laser energy. After laser irradiation, it is sustained with high temperature gradient, (We assume that the solidification velocity decreased with an increase of the temperature gradient in the melted region) so that liquid-phase growth occurred from the interface between liquid Si and c-Si substrate during re-crystallization. In addition, it can be estimated that the solidification velocity in the high laser energy regime became lower than that in the low laser energy regime, because the temperature of melt Si increased with an increase of laser energy. This estimation shows that there was little probability of nucleation during solidification in this laser energy regime. Accordingly, we considered that the nucleus density of initial growth may control the growth process. In the initial growth of grains, the nucleus may be the unevenness of the Si/SiO_2 interface or un-melted Si micro-crystals near the interface.

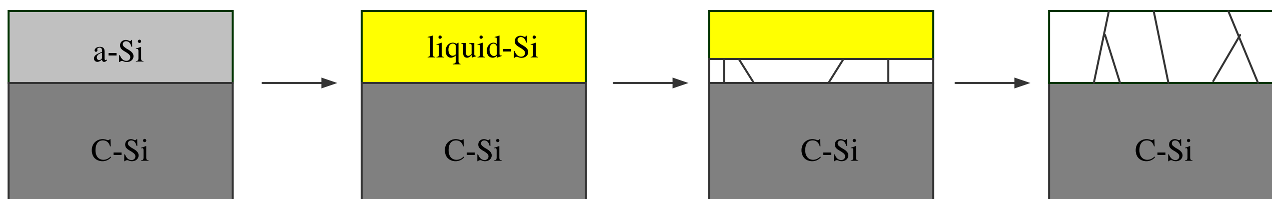

Fig. 2.14 The schematic representations of grain growth during laser irradiation, after laser irradiation and after recrystallization in the high laser fluence (0.4-0.5 J/cm^2)

2.7 Conclusions

We have used Raman spectroscopy to study the re-crystallization of a-Si by KrF excimer laser annealing. Our result shows that a laser fluence of 0.4 J/cm^2 is needed to re-crytallize the amorphous silicon layer. The Raman intensity of the c-Si peak at 520 cm^{-1} decreases due to attenuation by the amorphous silicon layer. The intensity of the c-Si Raman peak varies with the angle between laser polarization and silicon crystal orientation. Two methods, one utilizing directly the attenuation of substrate c-Si Raman signal by the amorphous layer and the other using the angle dependence of the c-Si peak, are used to calculate the thickness of amorphous silicon layer by Si ion implantation. The amorphous layer thickness was obtained with three different excitation wavelengths. Both methods yield consistent results without difference for the thickness of the a-Si layer, which is found to be around 18 nm and this value agrees well with results by other techniques. It demonstrates that Raman spectroscopy can be used to measure the thickness of the a-Si layer on c-Si substrate and it provides an effective solution to determine the thickness of thin film.

Our future work may be continued on samples with different PAI conditions and thus we could get different thickness of amorphous Si layers. With this determination method, we can approach not only junction depth, but also absorption co-efficient of amorphous layer.

References

1. D. J. Elliott: *Ultraviolet laser technology and applications* (Academic Press Inc, California, 1995) P209
2. A. Gat, L. Gerzberg, J. F. Gibbons, T. J. Magee, J. Peng and J. D. Hong: *Applied Physics Letters* 33 (1978) 775
3. T. Serikawa, S. Shirai, A. O Kamaoto and S. Suyama: *IEEE Transactions on Electron Devices* 36 (1989) 1929
4. T. Sameshima, S. Usui and M. Sekiya: *IEEE Electron Device Letters EDL*-7 (1986) 276
5. T. Saneshima, M. Hara and S. Usui: *Japanese Journal of Applied Physics* 28 (1989) 1789
6. R. Z. Bachrach, K. Winer, J. B. Boyce, S. E. Ready, R. I. Johanson and G. B. Anderson: *J. Electron. Mater*. 19 (1990) 241
7. C. P. Grigoropoulos, S. Moon, M. Lee, Appl. Phys. A 69 (1999) S295
8. S. Perkowitz: O*ptical Characterization of Semiconductors: Infrared, Raman and Photoluminescence Spectroscopy* (Academic Press Inc, California, 1993) P109
9. P. Dhamelincourt et M.Delhaye, *J Raman Spectrosc*. 22 (1991) 61
10. 10V. Wagner, W, Richter, J. Geurts, D. Drews, D.R.T. Zahn, *J Raman Spectrosc*. 27 (1996) 265
11. R. Ohr, C. Schug, *Anal. Bioanal.Chem*. 375 (2003) 47
12. Goto, K., Yamamoto, T, *International Electron Device Meeting* 1999, 931
13. G.Groos, M. Stutzmann, *Journal of Non-Crystalline Solids* 227-230 (1998) 938
14. T.Sameshima, S.Usui, *J. Appl. Phys.* 70 (1991) 1281

15. Z.Iqbal and S. Veprek, *J. Phys. C* 15 (1982) 377

16. A.K. Shukla, K. P. Jain. *Phys. Rev. B* 35 (1987) 9240

17. Hiroyuki Watanabe, Hirofumi Miki, Shigeru Sugai, Koji Kawasaki and Toshihide Kioka, *Jpn. J. Appl. Phys.* Vol. 33 (1994) 4491

18. Http://courses.nus.edu.sg/course/elengv/ee6503

19. Yong-Hae Kim, Chi-Sun Hwang, *Thin Solid Films* 440 (2003) 169

20. Reference for n and k data of Si: SI-JELL FROM JELLISON (3-1-91) MEASU

21. Edward D. Palik, Gorachand Ghosh, "*The electronic handbook of optical constants of solids"*, San Diego, CA, 1999

22. C.H. Poon, B. J. Cho, Y. F. Lu, M. Bhat, A. See, *J. Vac. Sci. Technol. B* 21 (2003) 706

23. E.P. Donovan, F. Spaepen, D.T. Turnbull, J.M. Poate and D. C. Jacobson: *Solid-State Electron.* 42 (1983) 698

Chapter 3 Theoretical estimations on nano-crystal

3.1 Theory of photoluminescence from nano-scale silicon

The origin of visible photoluminescence from nano-scale silicon is the subject of much debate. Thus it is necessary to review the theoretical model [1].

3.1.1 Effective mass model

The Effective Mass Model has been successfully applied to explain bulk semiconductor optical phenomenon. The effective mass model is a quasi-particle theory that treats the electron excited to the conduction band and hole created in the valence band as free particles, whose effective masses are determined by a quadratic fit to the curvature at the band minima (maxima) of the conduction (valence band). If we add to this picture the columbic attraction an electron and hole will feel, we have the theoretically simplest manifestation of an exciton. For a quantum dot this exciton presents an energy spectrum analogous to a hydrogen atom (i.e. with radial and angular quantum numbers) but it is further complicated by the fact it is in a thermal bath of phonons and that the "mass" of an exciton is energy dependent. Excitons eventually decay however, by electron hole annihilation, which can be accompanied by the emission of a photon (luminescence), with or without phonon absorption/emission or the acceleration of a free charge (Auger process). In bulk crystalline silicon without doping near 0K, the quantum yield of exciton formation approaches 1. Free carriers (the sites of non-radiative recombination) decrease this yield to a fraction of a percent at room temperature. The radiative lifetime for an exciton is quite long (~ms) due to the 2nd order nature of electron–hole recombination in

indirect semiconductors (the electron has to absorb a phonon and a hole). And so, at room temperature non-radiative processes move the decay lifetime to the μs to ns regime.

The increase in the radiative recombination rate may be understood as a consequence of Fermi's Golden Rule:

$$\frac{1}{\tau} \propto E_0 \left| \left\langle f \middle| \vec{p} \middle| i \right\rangle \right|^2 ,$$

where τ is the radiative lifetime, i is the initial state, f is the final state, and E_0 is the energy of the transition. Spatial confinement implies a widely spread representation in momentum space, increasing the magnitude of the optical matrix element of the transition, thereby decreasing the lifetime.

Bulk model predictions break down however when the size of the crystal is less than the exciton's Bohr radius (i.e. radius of lowest energy Bohr orbital). For Si this is 49Å [2] and CdSe it is 61Å[3]. Crystallites with diameters smaller than this are said to be in the Quantum Confined (QC) regime [4,5]. Quantum Confinement has two main consequences: 1) it causes a blueshift in the bandgap energy; 2) it increases the probability of overlap between the electron and hole (i.e. optical matrix element is larger) which increases the rate of radiative recombination. The blue shift can be understood as the extra discretized energy of confinement that must be overcome to promote an electron to the conduction band.

3.1.2 Theoretical difficulties in modeling Si nano-crystals

The very few number of unit cells which exist in these nano-crystals (lattice constant for Si=5.4Å) may seem to invalidate the electronic-band structure point of view, which is

accurate in describing bulk crystal spectra. Direct semiconductor nano-crystals like CdSe [6] and InAs have been quite successfully modeled [7] by effective mass theories. Significant quantitative deviations appear for nano-crystals below 1.5nm in size, though the main features of the spectra are qualitatively well descried by the theory's term assignments [8]. The ordering of those terms is different than traditional atomic spectra, which are solutions to an electron in a coulombic potential; the effective mass electrons of the CdSe or InAs have the additional constraint of being assumed to be in an infinite or square well potential.

Views are polarized between quantum confinement and other mechanisms. An explanation based on quantum size effects alone does not explain all observations. Surface species, surface states, and fabrication of wavelength and pore structure also play a role.

The overlap of wavefunctions has an especially dramatic effect for indirect type semiconductors like Si. In the bulk crystal the energy band representation in k space can be justified by periodicity. For nano-crystals, however, periodicity is lost and k is no longer a good quantum number. Confinement in real space implies that in reciprocal space the stationary states must be represented by a superposition of k states when expressed in the k basis. This allows transitions which were previously indirect to become direct-like under confinement [9,10].

In addition to the confinement effects, the surface too has an important bearing on the optical activity. For nano-crystalline materials the fraction of atoms that are on the

surface are significant, as opposed to bulk crystals. For this reason the structure and bonding at the surface must be considered.

Surfaces may be divided into two classes, passivated and un-passivated. Passivated surfaces have all their bonds bonded to another chemical species or semiconductor layer. This hybridization is what gives rise to the continuum of states in the conduction and valence bands that is approached in the bulk crystal. Un-passivated surfaces have surface bonds left dangling (i.e. left un-hybridized). Such dangling bonds have two consequences: i) they introduce states within the forbidden “band-gap” of the material, ii) they are sites of efficient non-radiative recombination. The mid-gap states arise since the unpaired bond cannot hybridize into the bonding and anti-bonding levels (or to the “valence” and “conduction” levels).

In addition to avoiding the above scenario, passivation is also a technique used to better localize the excitonic states. By surrounding a semiconductor with another of larger band-gap, localization is enhanced. This type of bandgap engineering has been used to great advantage in increasing the efficiency of quantum well lasers [11]. Mid-gap states can be generated by impurities (e.g. donor or acceptor atoms) in the bulk, but such effects will be ignored in nano-crystals since the probability of such an impurity to exist is negligible [12].

The coulombic exchange interaction has until recently been ignored in nano-crystal modeling efforts, though recent Monte Carlo simulations show it to contribute to a significant blue shift in the “band-gap” (self-energy correction)[13]. The exchange term

arises because the coulomb interaction term is not diagonal in the single particle basis. The mixing that arises is found to be enhanced by the quantum confinement.

One of the most challenging problems in understanding “indirect” nanocrystalline luminescence (i.e. Si, Ge) is finding a satisfactory explanation for the significant stokes shift that is observed (~1 eV for Si) upon band-edge excitation (i.e. at the absorption onset (~4 eV for Si)). This contrasts with “direct” nano-crystals semiconductors that have a negligible Stocks shift at the band-edge.

It is at this point that an explanation of “indirect” nano-crystals as being “direct”-like breaks down. Straightforward explanations due to an excited state lattice relaxation have been ruled out as being too minor an effect (~100meV shift for Si)[14]. The most successful theory which explains this shift has been propounded [15][16]. The existence of a self-trapped exciton (STE)(most likely on the surface), which is stabilized for sufficiently small Si nanocrystals (<1.8nm in diameter)[17]. The nano-crystalline substrate acts as an elastic medium that prevents the complete dissociation of the excited dimmer, and stabilizes a relaxed excited state dimmer which may radiatively decay to the ground state.

The STE emission is not observed in the bulk or for larger crystallites because it is a metastable state. Only with quantum confinement and the concomitant blue shift in the band gap found in the smallest crystallites (d<1.8 nm) does the STE state become the stable excited state from which decay may occur. The Stokes shift found by this model compares well to the experimentally found shift (~1eV).

3.2 Theoretical calculations

We will discuss the wavelength of light from silicon nano-crystal. Since the bandgap of Silicon is 1.12 eV whereas that of SiO_2 is 8.0 eV (much larger than 1.12 eV), we can assume Si embedded in SiO_2 as one dimension well with infinite-square potential. According to SchrÖdinger equation, this problem could be solved as following.

In contrast with classical mechanics, solutions of the SchrÖdinger equation exist only for certain discrete values of energy. We shall analyze a simple example such that the energy spectrum consists only of discrete bound state. This is the infinite square well potential, corresponding to the motion of a particle constrained by impenetrable walls to move in a region of width L, where the potential energy is constant. Taking this constant to be zero, and defining a=L/2, the potential energy for this problem is

$$V(x) = \begin{cases} 0, -a < x < a \\ \infty, |x| > a \end{cases}$$

As the potential energy is infinite at $x = \pm a$, the probability of finding the particle outside the well is zero. The eigenfunction (wavefunction) $\psi(x)$ must therefore vanish for $|x| > a$, and we only need to solve the SchrÖdinger equation inside the well. Moreover, since the wavefunction must be continuous, $\psi(x)$ must vanish at the constraining walls, namely

$$\psi(x) = 0 \quad \text{at } x = \pm a$$

SchrÖdinger equation for $|x| < a$ is simply

$$-\frac{\hbar^2}{2m}\frac{d^2\psi(x)}{dx^2} = E\psi(x)$$

Setting $k = (2mE/\hbar^2)^{1/2}$, the general solution is a linear combination of the two linearly independent solutions $\exp(ikx)$ and $\exp(-ikx)$ or, equivalently, of the pair of real

solutions $\sin kx$ and $\cos kx$. Here, it is convenient to use real solutions, so that we shall write the general solution in the form

$$\psi(x) = A\cos kx + B\sin kx, k = (2mE/\hbar^2)^{1/2}$$

Let us apply the boundary conditions. We find in this way that the following two conditions must be obeyed

$$A\cos ka = 0\,,\ B\sin ka = 0$$

It is clear that we cannot allow both A and B to vanish, since this would yield the physically uninteresting trivial solution $\psi(x) = 0$. Also, we cannot make both $\cos ka$ and $\sin ka$ to vanish for a given value of *k*. Hence, there are two possible classes of solutions. For the first class B=0 and $\cos ka = 0$, so that the only allowed *k* values are

$$K_n = \frac{n\pi}{2a} = \frac{n\pi}{L}$$

with n=1,3,5,···. The corresponding wave functions $\psi_n(x) = A_n \cos k_n x$ can be normalized so that

$$\int_{-a}^{+a} \psi_n^*(x)\psi_n(x)dx = 1$$

The normalized eigenfunctions of the first class can therefore be written as

$$\psi_n(x) = \frac{1}{\sqrt{a}}\cos\frac{n\pi}{2a}x\ ,\quad n=1,3,5,\cdots$$

In the same way, we find that the normalized eigenfunctions of the second class are

$$\psi_n(x) = \frac{1}{\sqrt{a}}\sin\frac{n\pi}{2a}x\ ,\quad n=2,4,6,\cdots$$

Taking into account the two classes of solutions, we find that the values of *k* are quantized, being given by $k_n = n\pi L$, with *n*=1,2,3,···. The energy eigenvalue is also quantized, being

$$E_n = \frac{\hbar^2 k_n{}^2}{2m} = \frac{\hbar^2}{8m}\frac{n^2\pi^2}{a^2} = \frac{\hbar^2}{2m}\frac{n^2\pi^2}{L^2} \quad (n=1,2,3,\cdots)$$

so that the energy spectrum consists of an infinite number of discrete energy levels.

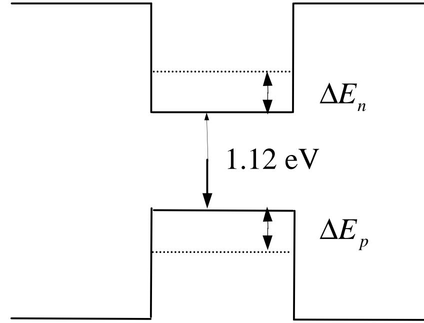

Fig. 3.1 Energy band diagram of silicon embedded with silicon oxide

Set n=1, $\Delta E_n = \frac{\hbar^2\pi^2}{2m_n R^2}$ (R is the radius of silicon nano-crystal)

Similarly, set n=1, we get $\Delta E_p = \frac{\hbar^2\pi^2}{2m_p R^2}$

For a particle in a box (infinite well) the energy spectrum due to this confinement is,

$$E_{confinement} = \frac{\hbar^2 n^2 \pi^2}{2ma^2}$$

Where a is the length scale of the confinement, n is the quantum number, and m is the effective mass. For a structure of size 1μm this zero-point confinement energy (i.e. for n=1) is ~10^{-6}eV. For nm sized structures this energy is significant (for optical transitions) ~1 eV.

As show in Fig. 3.1,

$$E_g = E_g^{Si} + \Delta E_g - \frac{1.8e^2}{\varepsilon R} \text{ [1]}$$

The first term is the bandgap of silicon, the second term is the change due to quantum confinement effect, the third term relates the columbic interaction between the electron and the lattice.

$$\Delta E_g = \Delta E_n + \Delta E_p = \frac{\hbar^2 \pi^2}{2m_n R^2} + \frac{\hbar^2 \pi^2}{2m_p R^2} = \frac{\hbar^2 \pi^2}{2m^* R^2}$$

$$\frac{1}{m^*} = \frac{1}{m_n} + \frac{1}{m_p} \ , \ \hbar = 1.05458 \times 10^{-34} Js \, , \ \pi = 3.14 \, , \ m_n = 1.18 m_0 \, , m_p = 0.81 m_0$$

$$m_0 = 0.91095 \times 10^{-30} kg \quad e = 1.6 \times 10^{-19} c \quad \varepsilon = 11.7$$

$$\Delta E_g = \frac{(1.05458 \times 10^{-34})^2 \times 3.14^2}{2 \times 0.91095 \times 10^{-30}} \left(\frac{1}{1.18} + \frac{1}{0.81}\right) \frac{1}{1.60218 \times 10^{-19}} \times \frac{1}{R^2 (10^{-9})^2} = 0.782 R^{-2} eV$$

$$E_g = 1.12 + 0.782 \times R^{-2} - 0.246 R^{-1} \times 10^{-10} eV$$

Plot E_g as a function of *R*, figure 3.2 (a) is obtained. It could be observed that the energy gap increases as the nano-crystal size decreases. According to $\lambda = hc / E_g$, plot wavelength as a function of crystal size, figure 3.2 (b) is obtained. As a result, wavelength of photoluminescence decreases as the nano-crystal size decreases. This gives us information that as long as we can fabricate crystal smaller than around 10 nm, photoluminescence occurs.

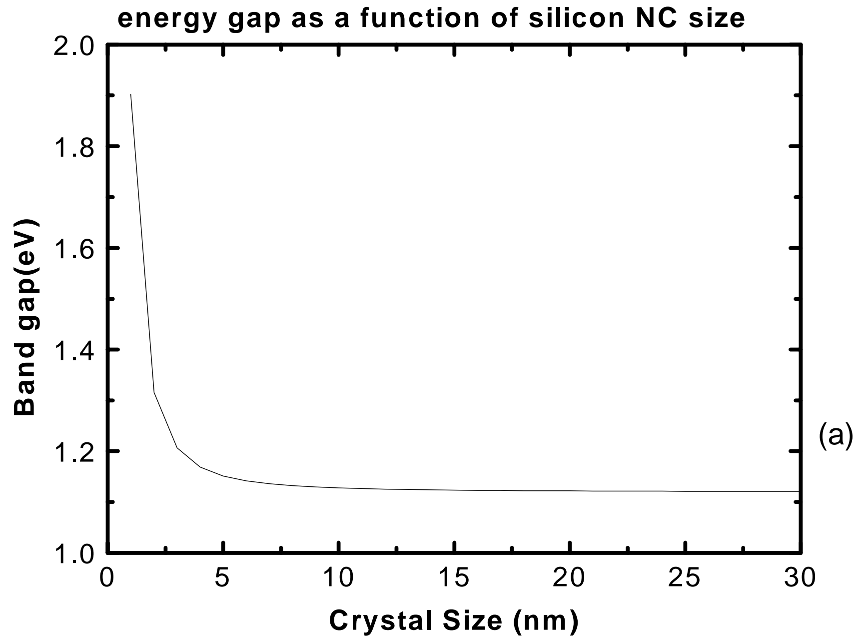

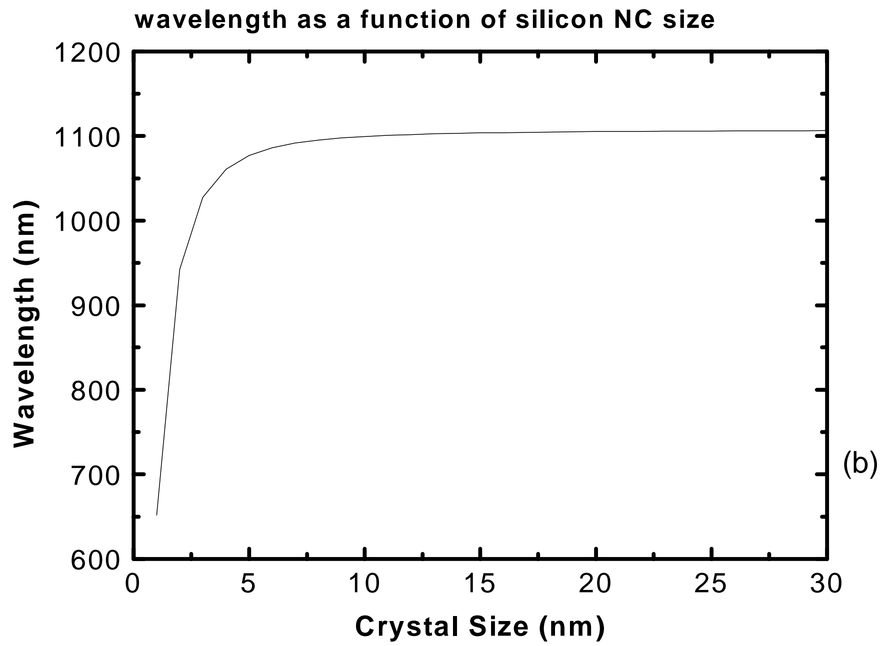

Fig. 3.2 Bandgap(a) and wavelength(b) as a function of crystal size

References

1. Http://www.physics.uiuc.edu/Research/Publications/theses/copies/akcakir

2. Cullis, A. G., Canham, L. T., and Calcott, P. D. J., *Journal of Applied Physics* 82 (3): 1997, 909

3. Grahn, H.T., *Introduction to Semiconductor Physics*, World Scientific, 1999

4. Klingshirm, C.G., *Semiconductor Optics*, Springer-Verlag, 1997

5. Nirmal, M., and Brus, L. *Acc. Chemical research*, 32, vol.5 (1999) 407

6. Norris, D. J., and Bawendi, M. G., *Physical Review B*, 53(24) (1996) 16338

7. Banin U., Lee C. J., Guzelian, A. A., Kadavanich, A. V., Alivisatos, A. P., Jaskolski, W., Bryant, G. W., Efros, A. L., Rosen, M., *Journal of Chemical Physics*, 109(6) (1998) 2306

8. Norris, D. J., Efros, Al.L., Rosen, M., and Bawendi, M.G. *Physical Review B*, 53 (24) (1996) 16347

9. Proot, J.P., Delerue, C., and Allan, G., *Applied Physics Letters*, 61(16) (1992) 1948

10.Delerue, C., Allan, G., and Lannoo, M., *Physical Review B*, 48 (15) (1993) 11024

11. Saleh, B.E.A, and Teich, M.C., *Fundamentals of Photonics*, John Wiley & Sons, 1991

12. Delerue, C., Allan, G., and Lanoo, M., *Physical Review B*, 48 (15) (1993) 11024

13.Ogut, S., Chelikowsky, R., and Louie, S.G., *Physical Review Letters* 97(9) (1997) 1770

14. Martin, E., Delerue, C., Allan, G., and Lanoo, M., *Physical Review B*, 50 (24) (1994) 18258

15. Allan, G., Delerue, C,m and Lanoo, M., *Physical Review Letters*, 76(16) (1996) 2961

16. Nayfeh, M. H., Rigakis, N., and Yamani, Z., *Physical Review B*, 56 (4) (1997) 2079

17.Wolkin, M.V., Jome, J., Fauchet, P.M., Allan, G., and Delerue, C., *Physical Review Letters*, 82 (1) (1999) 197

Chapter 4 Investigation on light emission from nano-scale Si

The focus of this chapter will be on the investigation of light emission mechanisms from nano-scale silicon.

4.1 Motivation for achieving silicon nano-crystals

4.1.1 Opto-electronics

LED based on nano-crystals offer many advantages for display applications as well as integrated optoelectronics. In particular, silicon nano-crystals may enable many advanced optoelectronic devices such as flat panel displays, semiconductor quantum dot lasers, and optical memories. Table 4-1 is the comparison of materials applied in photonic devices.

Table 4-1 Comparison of materials used in photonic devices

	III-V	GaN/ZnSe	SiC	C-Si	NC-Si
Efficiency	High	High	Low	Low	High
Wavelength	Infrared to green	Blue	Red to blue	Infrared	Controllable
Bandgap	Direct to indirect	Direct	Indirect	Indirect	Indirect
Integrate	Difficult	Difficult	--------	Easy	Easy
Cost	Expensive	Expensive	--------	Cheap	Cheap

As shown in the table, crystalline silicon suffers from a major disadvantage in that it can't be directly applied in optoelectronic devices because of its inherently poor luminescent properties. Fabrication of photonic devices with silicon is not suitable due to their extremely low efficiencies. In addition, it has an energy gap of inappropriate width. III-V

compounds had great success in the fabrication of LEDs with emission in the infrared to green. The key issue for the early success of these compounds was its direct band gap. However, one of the main challenges is that it will pose many problems to integrate them with the existing Si based microelectronics. Silicon carbide has been able to emit from the red to the blue spectral region. However, due to the indirect gap, radiative efficiencies are rather low. Promising direct band gap materials are ZnSe and GaN materials to produce a semiconductor that can emit blue light. However, these material systems suffer from a variety of shortcomings that include expensive processing and short operational lasing lifetimes. Another main problem is the lattice mismatch between Si and other materials that can be overcome but at a considerable cost.

New materials that luminesce efficiently are constantly being developed in the search for various device applications. However, there are several disadvantages with employing new materials. The most serious is in implementing with silicon electronic components. The lattice mismatch between silicon and new materials is generally not good and this eventually leads to device failure. Another major consideration in optoelectronic devices is the cost issues in manufacturing of these materials. The manufacturing of other materials is considerable more expensive in comparison to silicon. The lattice mismatch can be solved, but requires techniques that drive up the overall cost. Nevertheless, the potential use for new materials emitting efficiently in the visible spectral region can not be underestimated.

Nano-crystals have been the subject of much interest due to their efficient visible light emission properties that arise from quantum size effect as a direct result of their nanometer size. Nano-crystals or quantum dots (QD) are particles with physical

dimensions on the scale of a few nanometers and typically contain only a few thousand atoms or less. A considerable advantage of nano-crystal systems is the ability to control the emission wavelength. Semiconductor nano-crystals represent a novel form of crystalline materials that have attracted much attention due to their enhanced optical and electronic properties. Si nano-crystals are of particular technological importance due to the mature Si-based microelectronics industry. In addition, visible luminescence from silicon at low temperature was reported in 1984[1]. The considerable attention it has received recently is due to its ability to produce efficient luminescence at room temperature over a wide range of wavelengths, form the IR to green. Recent results suggest these observations may even extend into the blue. The drive towards higher performing optoelectronic systems demands a material capable of efficient light emission.

4.1.2 Single electron transistor (SET)

Unlike field-effect transistors, single electron devices are based on an intrinsically quantum phenomenon: the tunnel effect. This is observed when two metallic electrodes are separated by an insulating barrier about 1nm thick. In other words, it is just 10 atoms in a row. Electrons at the Fermi energy can “tunnel” through the insulator, even though in classical terms their energy would be too low to overcome the potential barrier. The electrical behavior of the tunnel junction depends on how effectively the barrier transmits electron waves, which decreases exponentially with its thickness, and on the number of electron-wave modes that impinge on the barrier, which is given by the area of the tunnel junction divided by the square of the electron wavelength. A single electron transistor exploits the fact that the transfer of charge through the barrier becomes quantized when the junction is made sufficiently resistive.

The single electron transistor can be viewed as an electron box that has two separate junctions for the entrance and exit of single electrons. It can be viewed as a field effect transistor in which the channel is replaced by two channel junctions forming a metallic island. The voltage applied to the gate electrode affects the amount of energy needed to change the number of electrons on the island. The island is often referred to as a quantum dot, since the electrons in the dot are confined in all three directions.

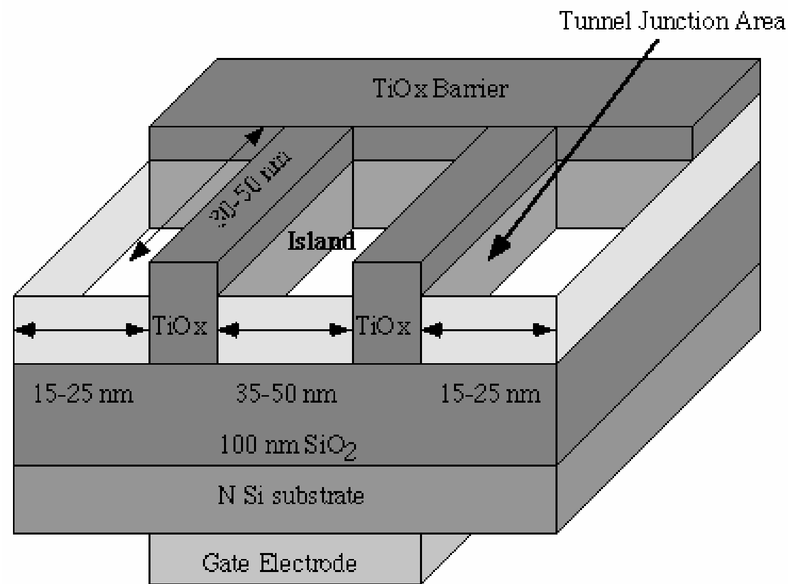

Fig. 4.1 Schematic of a single electron transistor

A schematic illustration of single electron transistor is shown in Figure 4.1. At both ends of the 3 nm thick Ti layer the source and drain ohmic contacts were formed, and on the back side of the n-Si substrate, the gate ohmic contact was formed. At the center region of the Ti layer, the island region was formed, surrounded by two parallel, narrow TiO_x lines, which serve as tunneling junctions for the SET, and two large TiO_x barrier regions.

For a SET to work at room temperature, the capacitance of the island must be less than 10^{-17} F and therefore its size must be smaller than 10 nm. Hence, silicon nano-crystal is a potential candidate for the island of SET.

4.2 Mechanisms of photoluminescence from silicon nano-structures

(1) Quantum confinement effect: The efficient luminescence arises from relaxation from energy levels created by the physical confinement of the charged carriers provided by the small dimensional crystalline structures. In spite of the enormous amount of research into the optical properties of P-Si (Porous Silicon), the mechanism and nature of efficient visible luminescence remain controversial. Although the mechanism for light emission remains under debate, the consensus is that crystalline nanometer structure in silicon is responsible. This school of thought suggests that carriers become physically confined within nanometer crystalline silicon structures left after electrochemical etching of Si. Carriers confined in low dimensional semiconductor structures behave differently than in their bulk counterparts. There are several reasons for this behavior. One reason is that low dimensional structures do not have an infinite periodic lattice. More importantly, the confinement of carriers by low dimensional structures modifies the band structure. In many systems this results in enhanced electronic and optical properties. This phenomenon is referred to as quantum confinement (QC). This field is well established for many low dimensional systems. However, there are other competing mechanisms that may be responsible for the observed light emission in P-Si and in other low dimensional Si structured systems that in turn complicate the analysis and therefore the interpretation.

(2) Defect: Luminescence originates from three kinds of defects, which are crystalline or surface defects, dangling bonds and photo-induced defects. Three main effects can be produced by oxidation [4]. First, oxygen induces passivation of the cluster surface by the saturation of dangling bonds. Thus it reduces the number of non-radiative recombination centers and, as a result, leads to the increase of luminescence intensity. The second effect

is the decrease of the cluster silicon core that should lead to the blue-shift of the luminescence band. The third effect is the increase of the amount of silicon oxide the sample which could lead to the appearance of luminescence from defects in the oxide layer or at the Si/SiO_x interface, or to an increase in its intensity if it already exists.

(3) Surface effects: luminescence may arise from states created by the large internal surface, or from states created by the surface/interface, or from molecular species that cover the P-Si surface.

(4) Silicon based species: silicon based species such as SiO_2, Siloxenes or siloxene derivatives, polysilanes, SiH_x, SiO_x and Si-F exhibit strong visible PL.

(5) Microcrystalline silicon: microcrystalline silicon structures have been shown to exhibit visible luminescence.

(6) Amorphous species: amorphous silicon and other amorphous species are present. Many researchers suggest that amorphous species such as a-Si and a-SiO_x are responsible for the observed luminescence.

(7) Impurities: recombination of electron-hole pairs can occur through impurities created during electrochemical etching of silicon.

4.3 Nano-scale silicon fabrications and typical results in literature

4.3.1 Porous silicon by electrochemical etching [2]

Porous silicon can be fabricated by electrochemical etching of silicon wafers in hydrofluoric acid. Either p or n type silicon wafers can be used. Porous silicon is produced by electrochemical etching with a constant current density of 20 mA/cm^2 in a 49wt % hydrofluoric acid (HF) solution for 20 minutes. Figure 4.2 shows the schematic of a conventional anodization cell. Various forms of P-Si can be obtained depending on the resistivity of the Si wafer as well as on the different etching conditions. The different forms of porous silicon as shown in Fig.4.3 emit in different spectral regions.

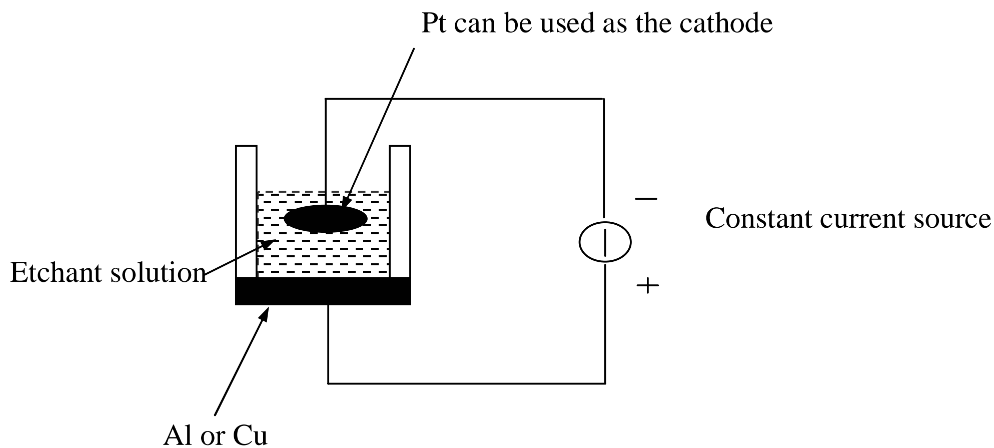

Fig. 4.2 Schematic of cell used for electrochemical etching of Silicon wafers in hydrofluoric acid [2]

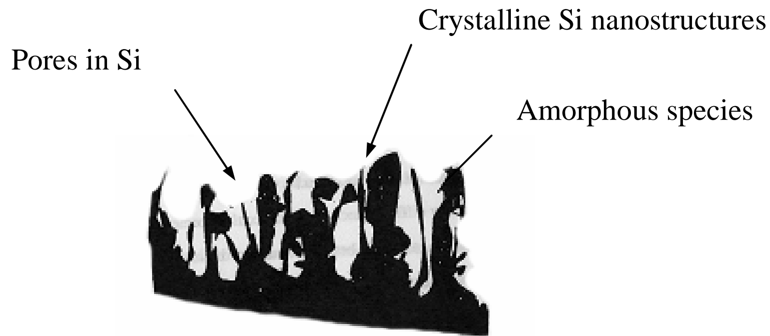

Fig. 4.3 The surface layer of porous silicon consists of nanometer size silicon structures. There are many nanometer size and shape crystalline silicon structures.

4.3.2 Silicon pillars and cones by ion etching [3]

The silicon cones were etched in silicon-on-insulator (SOI) wafers using rough Ag films as etch masks. SOI wafers were employed to create a wide bandgap layer below the fabricated Si nanostructures in order to enhance quantum confinement effects. The SOI (100) wafers featured a surface Si layer of thickness 200 nm separated from the bulk Si crystal by a 400 nm layer of SiO_2. Scanning Electron Microscopy of silicon cones is shown in Fig. 4.4.

Samples oxidized at 900˚C exhibit intense yellow/green photoluminescence centered at about 530 nm. STEM bright field micrograph of a silicon cone embedded in silicon oxide, produced by RIE of a SOI substrate and subsequent oxidation for 30 min at 900˚C, is shown in Fig. 4.5.

Samples oxidized at 1000˚C luminesce in the red-to-infrared region with peak positions between 650 to 730 nm. As shown in Fig. 4.6, transmission electron microscopy characterization is employed to show that PL at 530 nm can be understood in terms of

defect states, while the PL at 650-730 nm can be explained by a combination of defect states and quantum confinement effects.

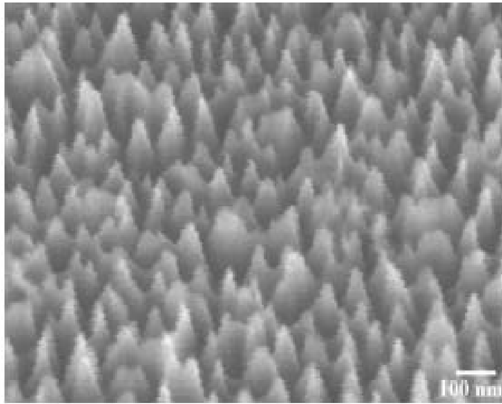

Fig. 4.4 Scanning electron micrograph of silicon cones fabricated by reactive ion etching of a silicon-on-oxide wafer (after cleaning) [3]

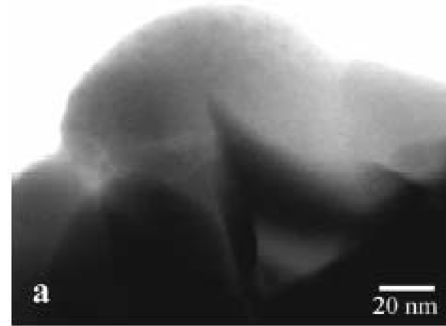

Fig. 4.5 STEM bright field micrograph of a silicon cone embedded in silicon oxide, produced by RIE of a SOI substrate and subsequent oxidation for 30 min at 900˚C[3]

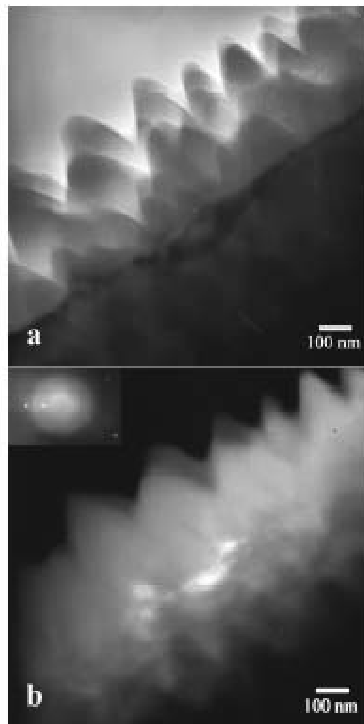

Fig. 4.6 Transmission electron micrograph of silicon cones etched in an SOI substrate and oxidized for 2 hours at 1000˚C [3]

Photoluminescence intensity increase during initial oxidation may be due to more defects being created than being annealed out. Subsequently the oxidation rate decreases due to the self-limiting effect in small silicon structures for temperatures below 950˚C, and the interface advances progressively more slowly. In this regime, more defects are annealed out than are induced by oxidation and the PL intensity decreases.

Photoluminescence from samples oxidized at 1000˚C arises from both defect states and quantum confinement.

4.3.3 Silicon nano-crystal prepared by silicon ion implantation into SiO_2 films [4]

The SiO_2 film was grown on 12-14 Ωcm, n-type Si (100) substrate by thermal oxidation at 900˚C. Oxide thickness was about 500 nm. Double implantation of Si ions at room temperature was used to produce an approximated uniform concentration profile. At first, Si ions with an energy of 160 keV were implanted into the oxide layer to doses of $5\times10^{16}/cm^2$ and then Si ions at 70 keV to doses of $3\times10^{16}/cm^2$. The samples were annealed at 400-1200˚C in a N_2 atmosphere for 30 min.

PL results show that the intensity of E_1 at 1.74 eV and E_2 at 1.96 eV decreases significantly with increasing annealing temperature. And the two peaks virtually disappear after thermal annealing at 800˚C**.** These PL peaks should originate from the defects in the SiO_2 layers caused by ion implantation. Many Si-O bonds in the SiO_2 layers are destroyed and the ratio of O/Si atoms is less than two after Si ion implantation so that some oxygen-deficient type defects are induced. Only the density of defects changes after annealing at

different temperature, so the intensity of the peaks decreases with annealing temperature but their position does not change.

The silicon nano-crystals are formed in the Si-rich matrix when the annealing temperature is raised above 900˚C. The size and density of silicon nano-crystals increase with increasing annealing temperature so that the position of the PL peak shifts to lower energy and its intensity increases.

4.3.4 Silicon nano-clusters with reduced size dispersion produced by laser ablation [5]

The Si nano-crystals were produced by conventional laser ablation. A mono-crystalline Si (100) or (111) sample was placed on a rotating target holder inside a stainless steel vacuum chamber coupled to an oil-free turbo-molecular pump. After pumping down to 1×10^{-7} Torr, a slow gas flow with a pressure varied from 1 to 4 Torr was induced into the chamber. This ambient gas was composed of pure He or of He with a little admixture of a reactive gas such as oxygen. A large condensation of Si nano-clusters with a reduced size dispersion was obtained by selecting the appropriate experimental parameters.

It was shown that by varying the cluster size in relation to experimental parameters it is possible to obtain different PL bands ranging from near ultraviolet (UV) to near infrared (IR). The size-independent photoluminescence of Si nano-clusters is consistent with a quantum confinement effect. The observed influence of cluster oxidation on the luminescence properties also supports the quantum confinement interpretation.

It was found that the distribution becomes narrower and its maximum shifts to lower sizes when the distance from the ablation spot increases. The cluster size was varied by changing the preparation conditions or the distance between the area of observation and the ablation spot. It was also seen that when the laser fluence increases, the luminescence band shifts to lower energies within a very wide spectral range from 3.5 to 1.7 eV, caused by the corresponding increase of cluster size, as shown in Fig.4.7 and Fig.4.8.

The luminescence intensity increases and apparent maximum of the luminescence bands shift slightly to the blue after oxidation. The change of the band intensity is more pronounced at the high-energy part of the spectrum and we can note the appearance of a weak additional oxide band. This indicates that the main contribution of oxidation corresponds to passivation of the cluster surface and reduction of cluster sizes. The radiative transitions between defect states of silicon oxide do not make a significant contribution to the luminescence. The blue shift of the emission band compared with that of un-oxidized Si clusters of the same initial size is then due to a quantum confinement of carriers in the crystalline Si core of reduced size.

4.3.5 Photoluminescence from silicon single quantum wells [6]

Wafers were formed by implanting $^{16}O^{+}$ with a dose of 1.8×10^{18} cm^{-2} at 200 keV followed by sintering at 1310˚C for 5 h and at 1350˚C for 40 h. The initial 140-nm superficial Si thickness was reduced to 3 nm or less by thermal oxidation from 900˚C to 1100˚C. The single quantum wells were sandwiched between SiO_2 layers.

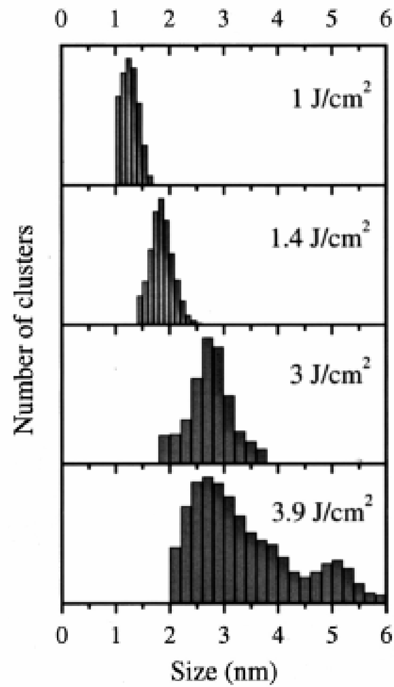

Fig. 4.7 Cluster size distribution for deposits prepared at 4 Torr of He and at different laser fluences [5]

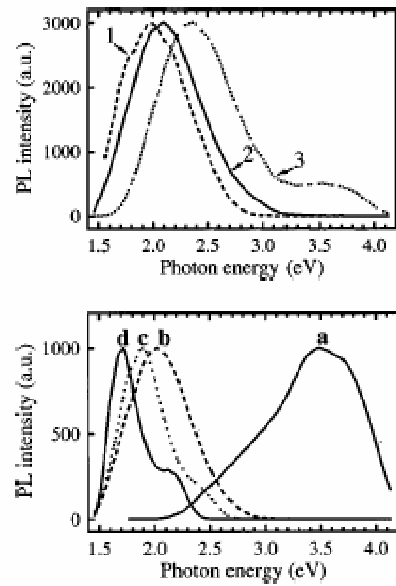

Fig. 4.8 (a)Photoluminescence spectra of silicon nano-clusters measured on different sites on the sample. From spectrum 1 to 3 the distance between the observation point and the ablation spot increases from 2 to 10 mm.
(b)Photoluminescence spectra of silicon nano-clusters performed at the center of the samples. Samples are prepared under 4 Torr of He at different laser fluences: (a) 1 (b) 1.4 (c) 3 (d) 3.9 J/cm^2 [5]

As shown in Fig.4.9, the PL spectrum exhibits a peak around 1.65 eV at 2 K. The PL spectrum from the Si quantum well is asymmetric and can be fitted by two Gaussian bands: The strong-intensity band and the weak one. The well-thickness dependence of the PL spectrum and PL dynamics measurements indicate that the strong PL band is ascribed to the radiative recombination in the Si-SiO_2 interface region and the weak band to the radiative recombination in the Si 2D quantum well. It was concluded that both the Si-SiO_2 interface states and the quantum confinement play an important role in the radiative recombination. Spectroscopic studies of 2D Si quantum wells help to clarify the PL

mechanism of Si nanocrystals and porous Si and to understand microscopic structures of Si/SiO_2 interface.

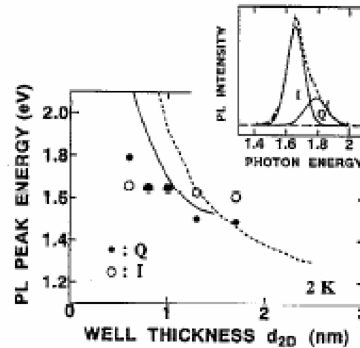

Fig. 4.9 PL peaks of Q and I bands as a function of Si well thickness. The solid and dotted lines are initial calculations of 2D-Si quantum confinement effects by Kageshima and by Zhang and Zunger respectively. The inset is the PL spectrum under the 2.540 ev excitation energy at 2 K in a 0.6 nm well thickness sample. The peak energy of fine structures is estimated by using Guassian functions and the solid lines represent the profiles, the Q band and the I band. [6]

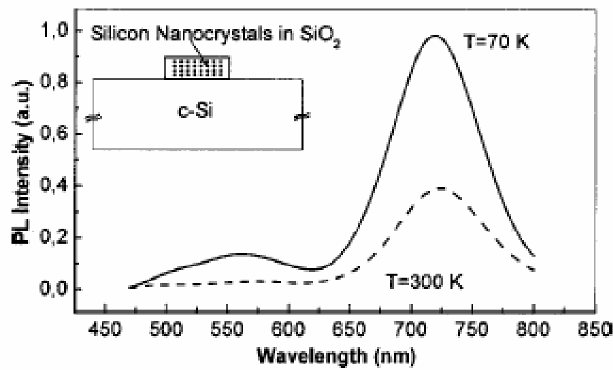

Fig. 4.10 PL spectra from silicon nanocrystals in a sample consisted of four $nc-Si/SiO_2$ bilayers at low different temperatures. The size of silicon nanocrystals was below 1.5 nm and they were not easily observed by TEM. SiO_2 thickness in each bilayer was 18 nm. Inset: Schematic of the $nc-Si/SiO_2$ multilayer structure. [7]

4.3.6 Silicon nanocrystals with sizes below 1.5 nm in Si/SiO_2 multilayers by LPCVD [7]

Samples were prepared by successive runs of low pressure chemical vapor deposition (LPCVD) of silicon on an initially oxidized silicon wafer and subsequent high temperature oxidation. The size of the silicon nano-crystals was below 1.5 nm, as verified by TEM results.

The experimental data shown in Fig. 4.10 are interpreted by considering two light emission mechanisms with closely similar wavelengths, both involving localized states and corresponding to two coupled subsystems. One involves localized states related to Si=O bonds, and the other self-trapped excitons. In the case of light emission from self-trapped exciton annihilation, PL was not limited by Auger recombination in the regime of multiple excitation of silicon nanocrystals.

4.3.7 Silicon nano-particles synthesized by laser-induced decomposition of silane [8]

Silicon nano-particles were produced by CO_2-laser-induced decomposition of SiH_4 mixed to helium in a controlled atmosphere reactor. By adjusting the pressure of both reactor and precursor gas and its dilution rate in helium, they were able to control, to an extent, the silicon growth rate and hence the particle diameter.

The photoluminescence spectra revealed two main peaks at about 1.7 eV and 2.1 eV. The peak position of the former was insensitive to the change of particle size, while its intensity increased after oxidation. The latter showed, however, a slightly size dependence but had undergone a drastic decrease after oxidation. They ascribed the red peak of 1.7 eV

to some radiative surface defect, while the yellow peak of 2.1 eV appeared consistent with an emission from an oxygen-related defect such as the non-bridging oxygen hole center.

4.3.8 Silicon nano-colloids [9]

Silicon nano-particles were produced by gas evaporation technique. The size of the particle was controlled by changing the He gas pressure. The formed nano-particles were trapped on the cryogenic matrix make of cold 2-propanol, which was used as a dispersing reagent because the high-purity sample was commercially available and dispersed colloidal suspensions were easily obtained.

The blue-green emission is found to be independent of size contrast to its intensity. The absolute quantum yield as a function of size is determined. From the proposed model that combines surface as well as volume effects, the emission is proved to be from a surface trapped site. The energy transfer efficiency form volume to the site is almost 100% for the 3.7 nm particle.

4.4 Challenges

(1) One of the main challenges encountered in realizing fully integrated light emitting devices is that semiconductors that emit efficiently in the visible are wide direct bandgap semiconductors which pose many problems for integrating with the existing silicon based microelectronics.

(2) The conceptual physics behind the optical properties remains a challenge.

4.5 Experimental details

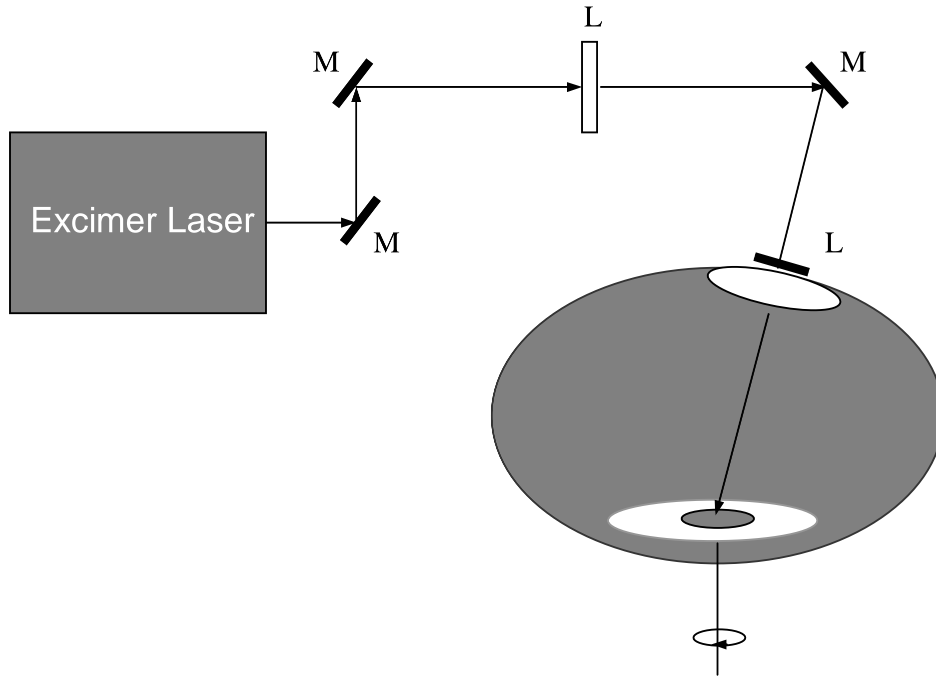

Fig. 4.11 Experimental diagram of laser ablation with silicon

In this work, silicon nano-structures, including network structures were produced by laser ablation. Photoluminescence spectra were investigated. We have successfully produced silicon nano-structures with high PL intensity. A key component in this work is the correlation between the optical properties observed and scanning electron microscopy analysis of the silicon structures, which allows us to determine the mechanism of emission, e.g. to distinguish between the roles of quantum confinement and oxide states.

N-type silicon wafer (100) was cleaned with toluene, aceton, and then with ethanol. It was subsequently put on top of a rotation stage. The stage was rotated at an angular velocity of 0.1 cycle/s. The schematic representation of the experiment is shown in Fig. 4.11. The UV laser, with the wavelength of 248 nm and pulse width of 23 ns, after passing through some mirrors and lenses, was introduced into the chamber, which were pumped to 4.8×10^{-6} Torr before being filled with ambient of argon or oxygen.

In order to understand the mechanism of light emission, several runs of laser ablation were repeated. The samples were prepared in vacuum, argon and oxygen with or without plasma. The total pressure of argon or oxygen was kept at 1.5 mTorr. The plasma condition was kept constant (with Ia=60mA, Ua=700V, P_f (Forward Power) =10mW, P_r (Reverse Power)=1mW). The silicon wafers were ablated by the UV light with the repetition rate of 10Hz and laser fluence of 5 J/cm^2 for 45 minutes.

Photoluminescence spectra were measured in air ambient immediately after fabrication with an argon laser (with the wavelength of 514.5 nm and the laser power of 25 mW) as the excitation light source. The wavelength cover range was selected from 517 nm to 874 nm. The luminescence of the sample was analyzed by a grating monochromator and detected by a CCD.

SEM pictures were taken with a Hitachi S-4100 field emission scanning electron microscopy (FESEM) machine. The acceleration voltage was 5 kV, and the emission current was 10 μA.

In order to further confirm the mechanism of the strong light emission from our sample prepared in oxygen, photoluminescence measurement with temperature range from 4 K to room temperature was carried out by pumping with a 488 nm line of an Ar^+ laser.

4.6 Experimental results and discussions

Figure 4.12 shows the photoluminescence spectra measured near the ablation area at samples prepared in vacuum, argon and oxygen with plasma respectively. Sample

prepared in oxygen ambient shows strong light emission while samples ablated in vacuum and argon give no light emission. The photoluminescence spectra measurement was

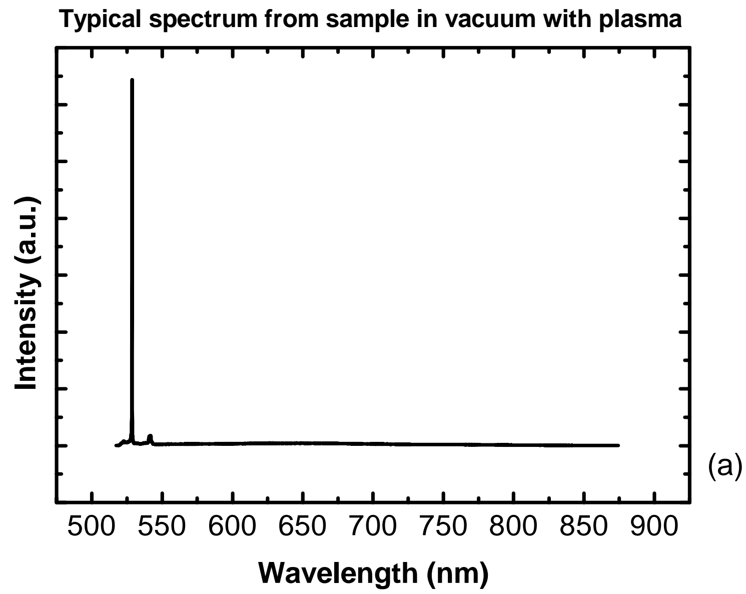

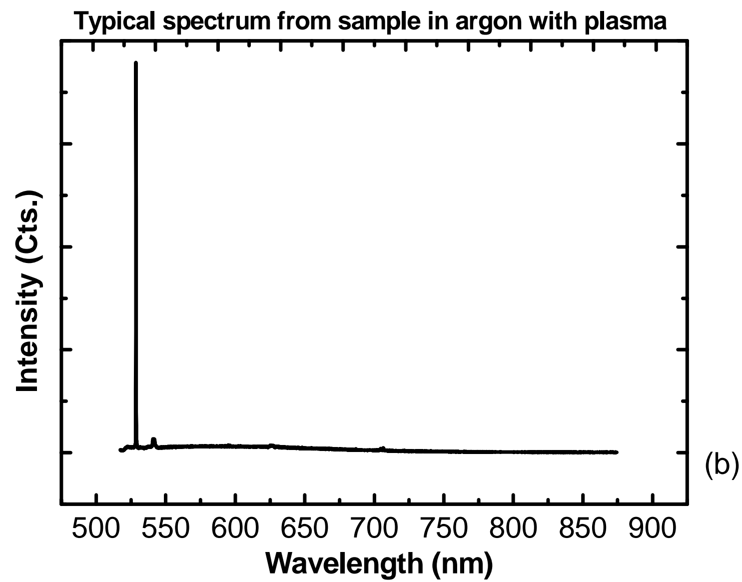

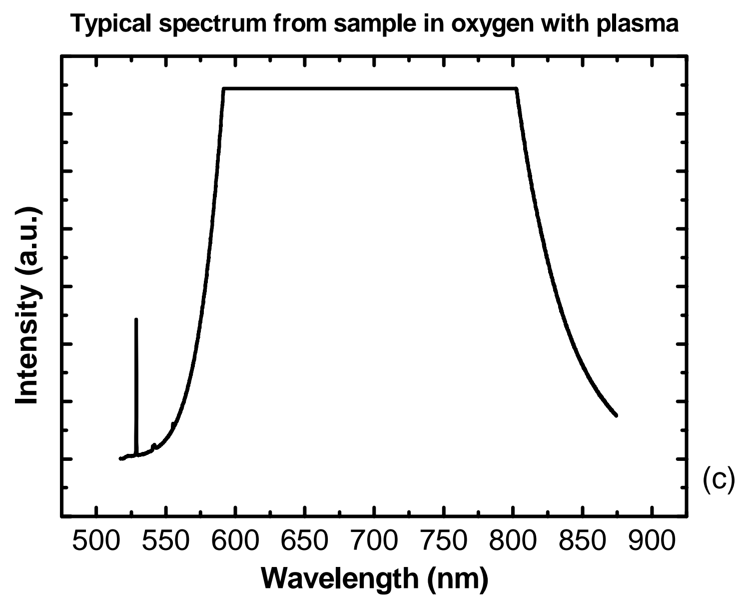

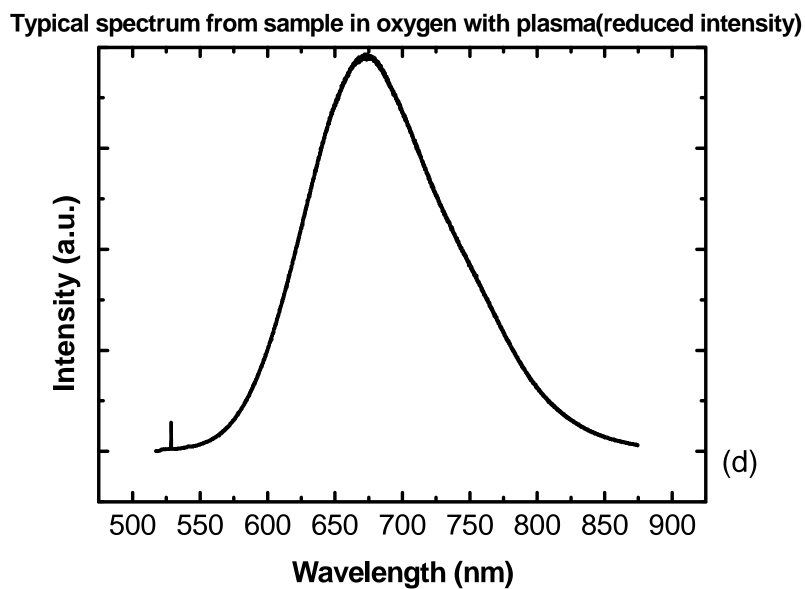

Fig. 4.12 Photoluminescence spectra obtained from samples prepared with plasma in (a) vacuum, (b) argon, (c) and (d) oxygen

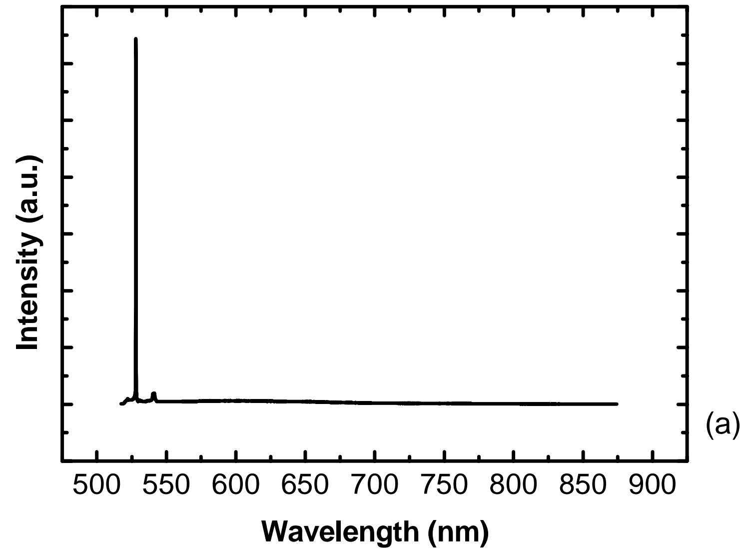
Typical spectrum from sample in vacuum without plasma
Intensity (a.u.)
500 550 600 650 700 750 800 850 900
Wavelength (nm)
(a)

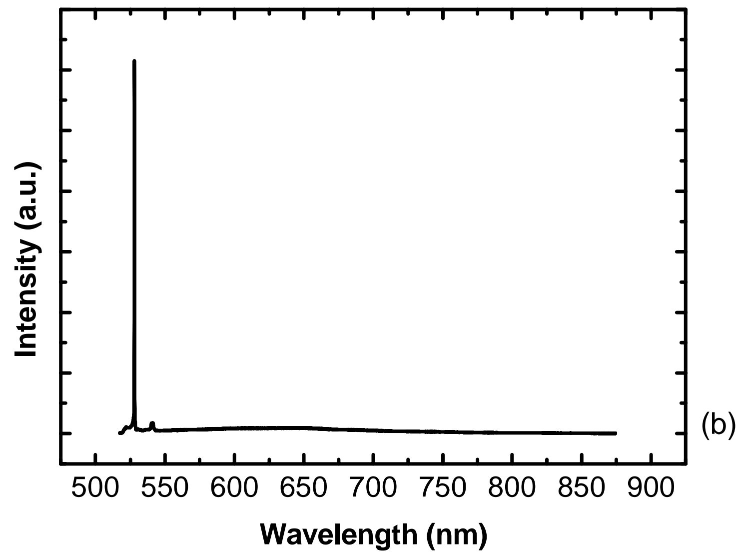
Typical spectrum from sample in argon without plasma
Intensity (a.u.)
500 550 600 650 700 750 800 850 900
Wavelength (nm)
(b)

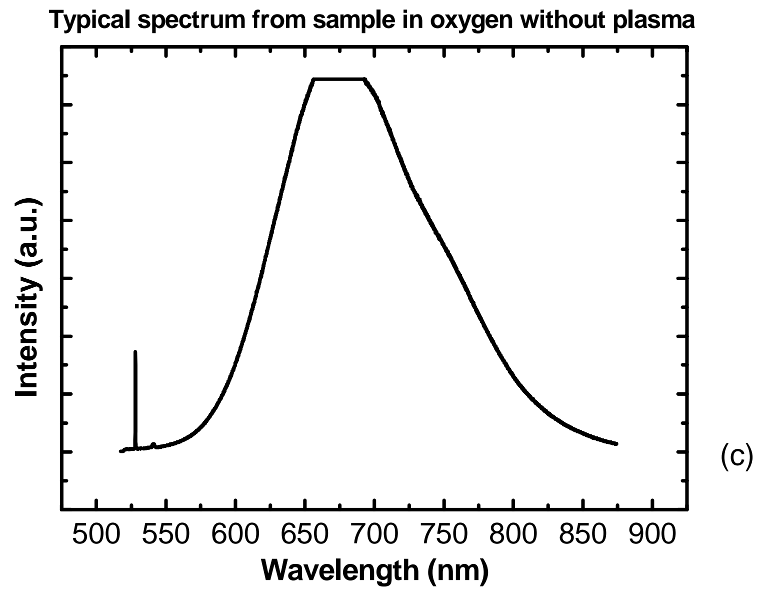

Fig. 4.13 Photoluminescence spectra obtained from samples prepared without plasma in (a) vacuum, (b) argon, and (c) oxygen

repeated with reduced laser power (using a light filter) so as to know the exact peak position. Peak ranging from 665 nm to 680 nm corresponding to 1.82 eV to 1.86 eV was observed. In order to rule out the influence of plasma, samples were prepared in vacuum, argon and oxygen but without plasma (we label them as A, B and C), which shows the same trend in PL spectra. As shown in the SEM pictures of Fig. 4.14 (a) and (b), sample A shows randomly distributed particles with various size in 2-μm-wide region while sample B shows random size particles but regularly distributed in 10-μm-wide region. It is due to the heavier argon, which is conventionally used as cooling down gas resulting in uniform and stationary plume of particles during the laser ablation [10]. To observe dramatic quantum confinement effects, the characteristic widths of Si-NC need to be significantly less than the dimensions of the free exciton Bohr radius of bulk silicon (a_B~5nm) [11-14]. As shown in fig. 4.13 (a) and (b), we did not observe any PL peak for sample A and sample B, which means that, these particles are not small enough to give light emission. As a result, quantum confinement effect does not apply to these two samples. To further investigate the mechanisms of light emission, these two samples are annealed at 900ºC in air ambient for three hours before we took the PL once again. As expected, still, no PL was observed. There are two possible explanations. One is that before oxidation, no Si-NC is smaller than 5 nm which does not meet the requirement for quantum confinement effect. The other is that after oxidation, for the large crystals, still no Si-NC is formed although much silicon was consumed and there is a SiO_2 shell outside the Si core [15-18]. Because of the self-limiting oxidation effect, oxidation stopped after some time when the core reaches a certain size, which is dependent on the initial silicon core size. Therefore, silicon core cannot reach the size required to give light emission. It is concluded that no light emission can be observed when the sample was prepared in vacuum or argon. This is

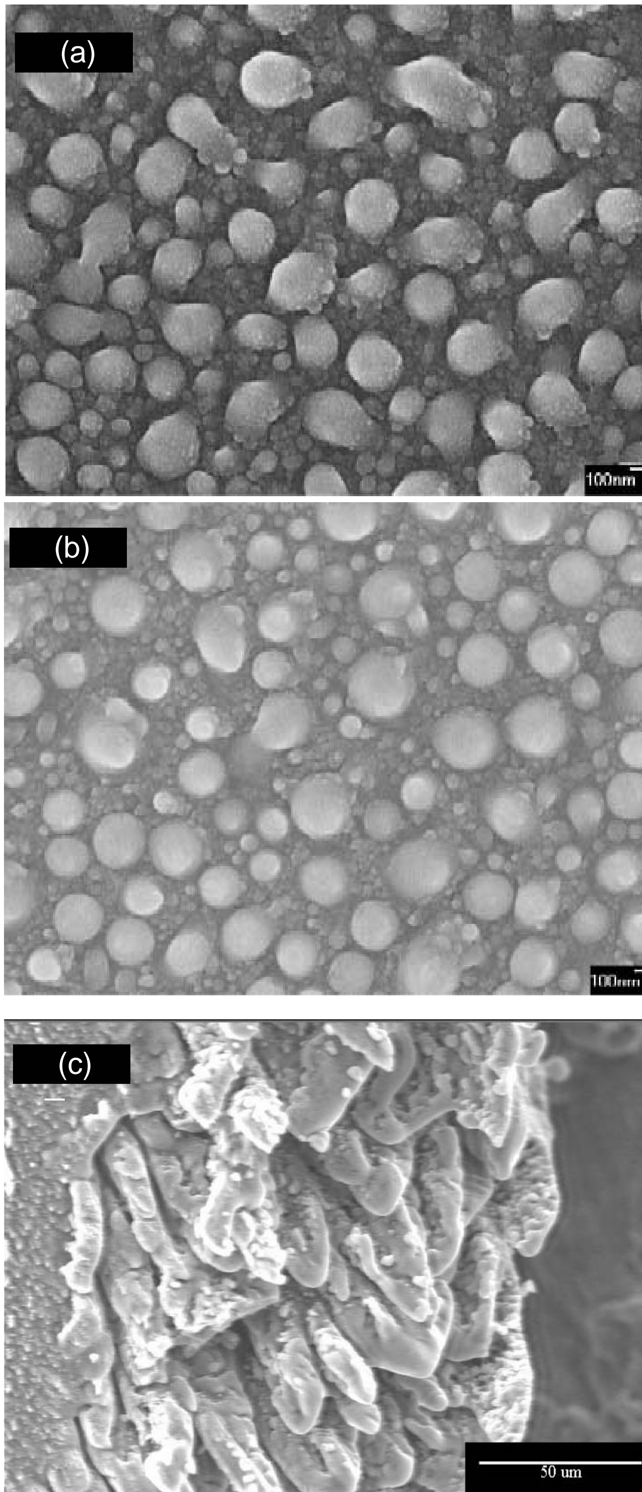

Fig. 4.14 SEM pictures from samples prepared in (a) vacuum and (b) argon (c) Oxygen in the ablation area

consistent with the previous literature [19,20] where laser ablation was carried out using silicon mixed powder as the target and c-Si target as a reference. It was found that it is much harder to get nano-scale silicon when using a c-Si under laser ablation condition compared to the silicon mixed powder as the target, which favors significantly the growth of nano-wires under pulsed laser ablation.

However, sample C, which is prepared in oxygen shows strong light emission, as shown in PL spectra of Fig. 4.13 (c). The broad spectra are due to the wide size distribution of the emitting crystallites. Although calculated band gaps of sub-1.5nm Si clusters extend from the blue to the ultraviolet (3-5eV)[21] and direct transitions in NC-Si have been reported [22], the blue-green and violet bands are most often associated with fast oxidation of P-Si or NC-Si during production or post processing treatments [23-25]. This is consistent with the visible light emission from our sample prepared in oxygen. The typical SEM picture of the laser ablation area is shown in fig. 4.14 (c). Small particles can be splashed off easily from the target surface. The particles with melted surfaces at the ablated spot are believed to form during the laser ablation. A columnar structure is a well-known phenomenon in laser ablation processing [26]. When the laser light is incident on the target surface, the deeper sites trap the radiation energy and cause a significant localized enhancement of the laser intensity and preferential splashing at the deeper sites. As the intensity of the laser increases such that there is significant melting and resolidification, the wave guide effect will become even more prominent and will lead to the formation of columnar structures and hollow channels. Figure 4.14(d)-(h) are SEM pictures observed from parts of the sample that show light emission. In order to see this more clearly, we

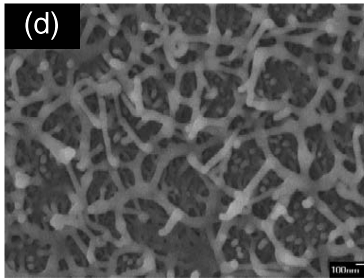

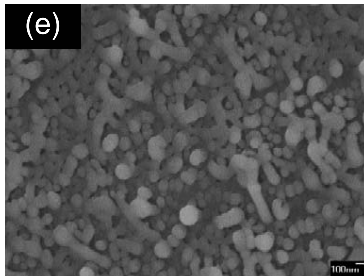

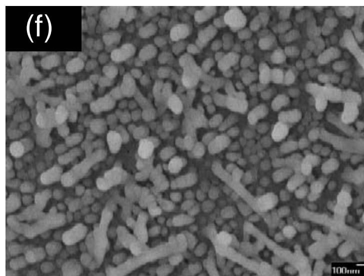

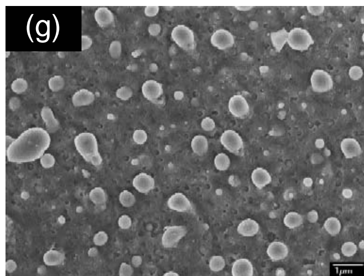

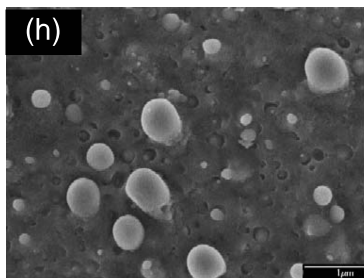

Fig. 4.14 (d)-(h) Typical structures that give light emission from sample prepared in oxygen

magnified (g) to (h). It can be observed from the SEM results that the size of Si/SiO_x ranges from 50 to 100 nm [27]. Red PL is divided into two categories: the models in which the luminescence occurs in quantum confined crystalline silicon nano-structures and the models in which it does not. Calculations within the effective mass approximation predicts that the object size leading to a bandgap in the "red" should be in the 2 to 4 nm range, depending on whether the crystallites are columnar or dot like [28,29]. Quantum confinement effect seems not to apply to our sample since we did not observe any size that meets the requirement. If such a small silicon core existed, the oxide shell should not form the large size (50 to 100 nm) due to the self-limiting oxidation effect [15].

Figure 4.15(a) shows SEM picture after dipped it into HF for 3 minutes and (b) is the corresponding PL spectrum that does not show any light emission. It is believed that light emission comes from the etched-off structure—Si enclosed by SiO_x. As a result, for the mechanisms of red PL from our sample, we can categorize them to the latter models. It is oxygen that plays a key role in the light emission from our sample. Bulk silicon oxide is known to luminesce efficiently in the visible under appropriate conditions but it is at a higher photon energy located at 4.1 eV [30], not 1.85 eV. Therefore, we can rule out this possibility. One probable mechanism that may contribute to the luminescence is the defects present at interface of Si/SiO_x, non-bridging oxygen hole center configuration in glass has been studied and shown to produce luminescence near 1.7-1.8 eV [31], which is consistent with our result. Rehm *et al* [32] used methanol to change the environment since methanol has the ability to penetrate the pores of a hydrogen passivated sample which lowers the energy barriers that exists between particles in the quantum confined crystallites. However, this method does not apply to our sample due to the oxide layer that protects the silicon crystallites from methanol penetration. We explain the

luminescence mechanism as follows. Since samples prepared in vacuum and argon (Sample A and Sample B) did not show any luminescence, one would expect it is the oxygen during the sample preparation that plays a much important role in the mechanism (as referred to figure 4.13 (c)), as can be referred in [33], where PL from oxidized porous silicon were observed from gas-suspended nano-particles. In both structures, the photoluminescence peaks should originate from the defects in the Si/SiO_2 interfaces. Si-O bonds may be induced when the sample is prepared in oxygen ambient. Oxygen induces passivation of the cluster surface by saturation of dangling bonds. Thus it reduces the number of non-radiative recombination centers and as a result leads to the increase of luminescence intensity. The HF attack results in a complete or almost complete removal of the oxide layers along with the silicon core. Luminescence comes from the Si/SiO_2 that has been etched since oxidation of the residual part cannot give light emission. It is the interface between Si and SiO_2 that creates levels in the middle of SiO_2 band-gap. The electron relaxes into these traps and emits in the red. Previous study also shows that the thickness of oxide shell is approximately 10% of the total particle diameter [34]. All the behaviors of PL were explained as resulting from a shrinking crystalline core and a growing oxide shell.

Figure 4.16 shows PL spectra as a function of temperature with excitation at 488 nm. The PL signal is much weaker than the spectra with the excitation source at the wavelength of 514.5 nm (as shown in fig.4.13 (c)). It is evident that the stokes-shift depends on the excitation energy [35, 36]. We can conclude that the large stokes-shift is mainly caused by exciton-phonon interactions [37,38]. The spacing between Gaussian peaks is approximately 500 meV, which is larger than the reported energy 135 meV [39] and 57 meV of TO phonons in crystalline silicon [40, 41]. This large difference cannot be simply

explained by the exciton-phonon, coupling in the Si crystallites as excitons are highly delocalized within the nano-crystals and fine structures do not correspond to phonon spectra in bulk Si. Therefore, we propose the luminescence is due to the strong coupling of excitons and local vibrations, which are usually observed in isolated small molecules at room temperature [42] where the coupling of excitons and surface silicon oxide vibrations are expected to increase with localization of excitons in smaller dimensions.

It was observed that there are three main peaks. One is a broad peak located at the higher energy, the other two are located at about 659 nm and 685 nm. A blue-shift of the broad peak is observed as the temperature is raised from 4 K to 197 K, while a red-shift is observed from 201K to 293 K. It can be explained as follows. In conventional fermion systems such as metals or partially filled valence or conduction bands in semiconductors, DOS (density of states) changes slowly around the chemical potential at 0 K, so chemical potential changes slowly with T. In the low energy tail of a Gaussian or other similarly broadened DOS, DOS increases approximately exponentially with energy and therefore chemical potential changes rapidly with T. For the low temperature range [43], the chemical potential is near the peak of the luminescence and the Fermi-Dirac distribution must be used to accurately match the expected data. At high temperatures, chemical potential is in the low energy tail of the luminescence, Maxwell-Boltzman distribution is a good approximation. The smaller red shift at high temperatures is consistent with the band gap energy shift of Si with temperature and some thermal broadening associated with the increase in thermal energy [44]. This result also supports the idea that confined excitons may be involved in the radiative process [45].

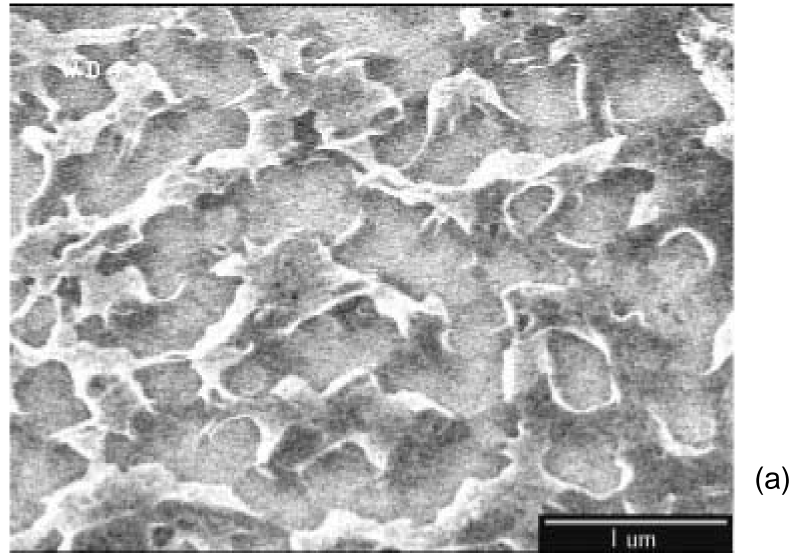

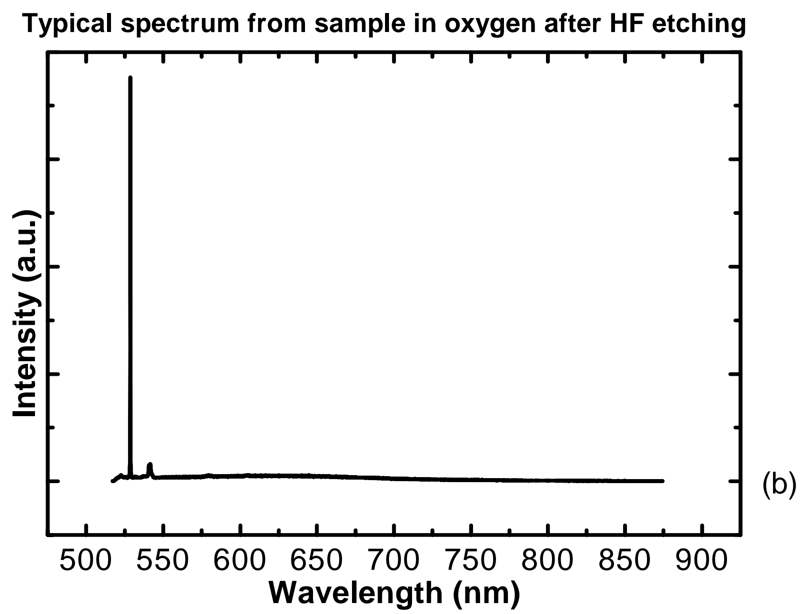

Fig. 4.15 (a) SEM picture and (b) Typical PL spectrum from sample prepared in oxygen after HF etching

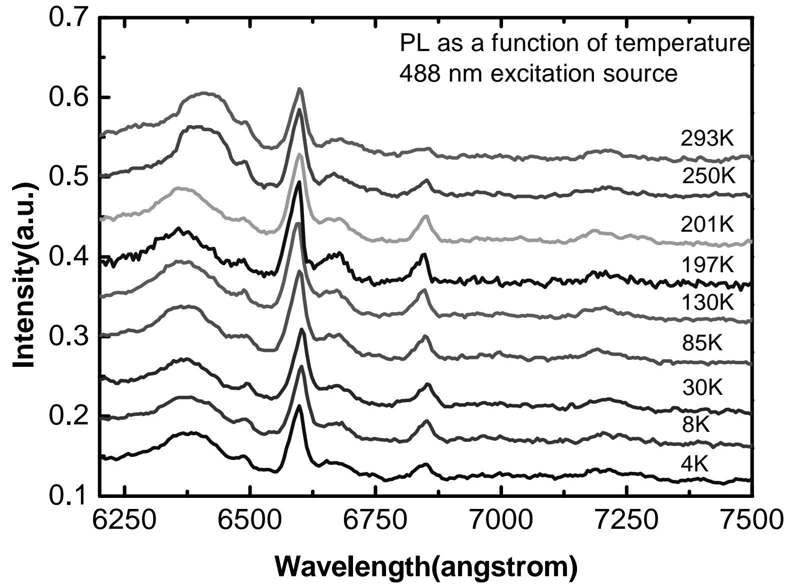

Fig. 4.16 PL spectra as a function of temperature with excitation at 488 nm

4.7 Conclusion

In this study, we have developed a new method to prepare silicon nano-structure that shows strong light emission. Oxygen is most important to the preparation. It is the interface of Si/SiO_2 that is of much importance to the luminescence. Silicon oxide introduces defects that increase the probability of recombination. This may provide a new way to fabricate structure with high light emission, which distinguishes from conventional techniques by its simple method and strong intensity.

4.8 Future work

We have done several runs of the production at different preparation conditions. Various structures that give strong light emission were obtained. It was found that structure that gives light emission could only be obtained at a critical value of laser fluence. Higher and lower fluences do not work. However, it is regretful that we did not obtain an exact rule.

It was also observed that the strong light emission from almost all of our samples quenched after some time. We cannot explain why. Previous literature shown that photoluminescence with more intensity and higher emission energy could be observed due to the oxidation of silicon nano-crystals. This is contradicted to our results. The real mechanism behind it needs further investigation.

Different parameters may still be tried in our future fabrication work, such as laser fluence and ablation time. The cluster size would be varied by changing the preparation conditions or the distance between the area of observation and the ablation spot. Lower fluence and larger distance could result in smaller cluster size.

Theoretical simulation on laser interaction with material may also be carried out to simulate the whole process.

References

1. C. Pickering, M. I. J. Beale, D. J. Robins, P. J. Pearson, And R. Greef, “Optical Studies of the Structure of Porous Silicon Films formed in p-type Degenerate and non-degenerate Silicon,” J. Phys. C: *Solid State Physics* 17 (1984) 6535
2. Gildardo Rios Delgado, thesis “ Investigation of Quantum Confinement in Silicon and Germanium Semiconductor Nanocrystals and their Application in Photonic Devices” UMI Company, August 1997
3. A. Wellner, R. E. Palmer, J.G. Zheng, C. J. Kiely, K. W. Kolasinski, *J. Appl. Phys.* 91 (2002) 3294
4. G. H. Li, K. Ding, Y.Chen, H.X. Han, and Z.P. Wang, *J. Appl. Phys.* 88 (2000) 1439
5. L. Patrone, D.Nelson, V.L.Safarov, M. Sentis, and W. Marine, *J. Appl. Phys*. 87 (2000) 3829
6. Shinji Okamoto and Yoshihiko Kanemitsu, *Solid State Communications* 103, No.10 (1997) 573-576
7. B.V. Kamenev and A. G. Nassiopoulou, *J. Appl. Phys.* 90 (2001) 5735
8. S. Botti and R.Coppola, *J. Appl. Phys*. 88 (2000) 3396
9. Keisaku Kimura and Shingo Iwasaki, *J. Appl. Phys*. 83 (1998) 1345
10. David B. Geohegan etal, *Appl. Phys. Lett.*, Vol. 72, No. 23 (1998) 2987
11. D. J. Lockwood, Z. H. Lu and J. M. Baribeau, *Phys. Rev. Lett.*, Vol 76, No. 3 (1996) 539
12. D.J. Lockwood, G. C. Aers, L.B. Allard, B. Bryskiewicz, S.Charbonneau, D. C. Houghton, J. P. Mccaffrey and A.Wang, *Can. J. Phys.* 70 (1992) 1184
13. C.Delerue, G.Allan and M. Lannoo, *Phys. Rev.B*, Vol. 48, No. 15 (1993) 11024

14. F. Buda, J. Kohanoff and M. Parrinello, *Phys. Rev. Lett.* Vol. 69, No. 8 (1992) 1272

15. Technical Proceedings of the 2000 International conference on Modeling and Simulation Microsystems MSM 2000

16. S. Schluppler, S.L. Friedman, M. A. Marcus, D. L. Adler, and Y. H. Xie, *Phys. Rev. B*, Vol 52, No. 7 (1995) 4910

17. Toshihide Takagahara and Kyozaburo Takeda, *Phys. Rev. B*, Vol. 46, No. 23 (1992) 15578

18. Sedar Ogut and James R. Chelikowsky, Phys. Rev. Lett. Vol. 79, No. 9 (1997) 1770

19. *Solid State Communications*, Vol. 105, No.6 (1998) 403

20. Y.F. Zhang, Y. H. Tang, C. S. Lee, N. Wang, I. Bello, S.T. Lee, *Journal of Materials Science Letters*, Vol. 18 (1999) 123

21. J. P. Proot, C. Delerue, and G. Allan, *Appl. Phys. Lett.* 61, 1948 (1992); T. Takagahara and K. Takeda, *Phys. Rev. B* 46 (1992) 15578

22. X, Zhao, O. Schoenfeld, S. Komuro, Y. Aoyagi, and T. Sugano, *Phys. Rev. B* 50, (1994)18654; *Jpn. J. Appl. Phys.*, Part 2 33 (1994) L899

23. Broad reviews have recently been given by P.M. Fauchet, J. Lumin. 70, (1996)294; F. Koch and C. Petrova-Koch, *J. Non-Cryst. Solids* 198-200 (1996) 846

24. R.E.Hummel, M. H. Ludwig, S.S. Chang, P.M.Fauchet, Ju. C.Vandy-shev, and L.Tsybeskov, *Sold State Communi.* 95 (1995) 553

25. K. Kim, M. S. Suh, T S. Kim, C.J. Youn, E.K. Suh, Y.J. Shin, K.B. Lee, H.J. Lee, M. H. An, H. J. Lee, and H. Ryu, *Appl. Phys. Lett.* 69 (1996) 3908

26. J. F. Ready, in "Effects of high power laser radiation", (Academic Press, New York,1997)

27. Philippe M. Fauchet, *Journal of Luminescence*, 70 (1996) 294

28. J. P. Proot, C. Delerue and G. Allan, *Appl. Phys. Lett.*61 (1992) 1948

29. L. W. Wang and A. Zunger, *J. Chem. Phys.* 100 (1994) 2394

30. A. Kux, D. Kovalev and F. Koch, *Appl. Phys. Lett.* 66 (1995) 49

31. S.Prokes, *Appl. Phys. Lett.* 62 (1993) 3244

32. J.M. Rehm and G. L. Mclendon, *Appl. Phys. Lett.* 66 (26) (1995) 3669

33. David B. Geohegan, Alex A. Puretzxy, Gerd Duscher, and Stephen J. Pennycook, *Applied Physics Letters*, Vol 73, No. 4 (1998) 438

34. Gilles Ledox, Jiong Gong et al, *Appl. Phys. Lett.* 79 (2001) 4028

35. Yoshihiko Kanemitsu and Nanoya Shimizu, *Phys. Rev. B*, Vol. 54, No. 20 (1996) 14329

36. A.Bsiesy, J. C. vial et al, *Surf. Sci*. 254 (1991) 195

37. E. Martin, C. Delerue, G. Allan, M. Lannoo, *Phys. Rev. B* 50 (1994) 18258

38. T. Takagahara and K. Takeda, *Phys. Rev. B* 53 (1996) R4205

39. Yoshihiko Kanemitsu and Nanoya Shimizu, *Phys. Rev. B*, Vol. 54, No. 20 (1996) 14329

40. P. D. J. Calocott, K. J. Nash, *J. Lumin.* 57 (193) 257

41. T.Suemoto, K. Tanaka, *Phys. Rev. Lett.* 70 (1993) 3659

42. M. Pope and C. E. Swenberg, *Electronic processes in organic crystals* (Clarendon, Oxford, 1982)

43. J.A. Kash, M. Zachau, E.E. Mendez, and J. M. Hong, *Phys. Rev. Lett.* Vol. 66 (1991) 2247

44. D.J. Lockwood, *Can. J. Phys.*, 70 (1992) 1184

45. S. Gardelis, J. S. Rimmer, P. Dawsoh, B. Hamilton, R. A. Kubiak, T. E. Whall and E. H. C. Parker, *Appl. Phys. Lett.* 59 (1991) 2118

Publications:

1. **Y.P. Zeng**, Y.F. Lu, Z.X. Shen, J.N. Zeng, W.X. Sun, B.J. Cho, C.H. Poon

Raman Spectroscopy Investigation on Excimer Laser Annealing and Thickness Determination of Nanoscale Amorphous Silicon (Published in Journal of Nanotechnology, 2004)

2. **Y.P. Zeng,** Y.F. Lu, J.N. Zeng and Z.X. Shen

Excimer Laser induced recrystallization and thickness determination of amorphous silicon layer using Raman spectroscopy (Accepted by Dec, 07~12, 2003 ICMAT, Symposium M)

3. **Y.P.Zeng**, Y.F. Lu, Z.X. Shen, X.Y. Chen

Photoluminesence from nano-scale silicon prepared by Excimer Laser

(To be submitted)

4. Chen XY, Lu YF, Cho BJ, **Zeng YP** et al,

Pattern-induced ripple structures at silicon-oxide/silicon interface by excimer laser irradiation

APPL PHYS LETT 81 (7): 1344-1346 AUG 12 2002